SIAM J. SCI. COMPUT.
Vol. 42, No. 4, pp. B951–B982

A COUPLED MULTIPHYSICS MODEL AND A DECOUPLED STABILIZED FINITE ELEMENT METHOD FOR THE CLOSED-LOOP GEOTHERMAL SYSTEM*

MD. ABDULLAH AL MAHBUB†, XIAOMING HE‡, NASRIN JAHAN NASU§, CHANGXIN QIU¶, YIFAN WANG‖, AND HAIBIAO ZHENG#

Abstract. The purpose of this article is to propose and analyze a new coupled multiphysics model and a decoupled stabilized finite element method for the closed-loop geothermal system, which mainly consists of a network of underground heat exchange pipelines to extract the geothermal heat from the geothermal reservoir. The new mathematical model considers the heat transfer between two different flow regions, namely the porous media flow in the geothermal reservoir and the free flow in the pipes. Darcy's law and Navier–Stokes equations are considered to govern the flows in these two regions, respectively, while the heat equation is coupled with the flow equations to describe the heat transfer in both regions. Furthermore, on the interface between the two regions, four physically valid interface conditions are considered to describe the continuity of the temperature and the heat flux as well as the no-fluid-communication feature of the closed-loop geothermal system. In the variational formulation, an interface stabilization term with a penalty parameter is added to overcome the difficulty of the possible numerical instability arising from the interface conditions in the finite element discretization. To solve the proposed model accurately and efficiently, we develop a stabilized decoupled finite element method which decouples not only the two flow regions but also the heat field and the flow field in each region. The stability of the proposed method is proved. Four numerical experiments are provided to demonstrate the applicability of the proposed model and the accuracy of the numerical method.

Key words. finite element method, stabilization, closed-loop geothermal system, heat transfer, porous media flow, channel flow

AMS subject classifications. 76R10, 76S05, 65N55, 65N30, 35Q35

DOI. 10.1137/19M1293533

1. Introduction.

As one major type of green energy, geothermal energy is renewable, independent of the weather or climate condition, environment-friendly, and

*Submitted to the journal's Computational Methods in Science and Engineering section October 15, 2019; accepted for publication (in revised form) April 22, 2020; published electronically July 28, 2020.

https://doi.org/10.1137/19M1293533

Funding: The work of the first, third, and sixth authors was partially supported by the NSF of China through grants 11571115 and 11971174, by the NSF of Shanghai through grant 19ZR1414300, and by the Science and Technology Commission of Shanghai Municipality through grants 18dz2271000 and 19JC1420102. The work of the second author was partially supported by the NSF through grant DMS-1722647.

†School of Mathematical Sciences, East China Normal University, Shanghai Key Laboratory of Pure Mathematics and Mathematical Practice, Shanghai 200241, People's Republic of China, and Department of Mathematics, Comilla University, Comilla 3506, Bangladesh (52150601021@stu.ecnu.edu.cn, dipmahbub13@yahoo.com).

‡Corresponding author. Department of Mathematics and Statistics, Missouri University of Science and Technology, Rolla, MO 65409 (hex@mst.edu).

§School of Mathematical Sciences, East China Normal University, Shanghai Key Laboratory of Pure Mathematics and Mathematical Practice, Shanghai 200241, People's Republic of China (52160601024@stu.ecnu.edu.cn).

¶Department of Mathematics, Iowa State University, Ames, IA 50011 (cxqiu@iastate.edu).

‖Department of Mathematics, University of California Berkeley, Berkeley, CA 94701 (qcutexu@berkeley.edu).

#Corresponding author. School of Mathematical Sciences, East China Normal University, Shanghai Key Laboratory of Pure Mathematics and Mathematical Practice, Shanghai 200241, People's Republic of China (hbzheng@math.ecnu.edu.cn).

widespread; hence it can significantly contribute to sustainable energy use [82, 38, 17]. One major technique to extract the geothermal energy is the closed-loop heat exchanger, which circulates working fluid down to the rock mass with high temperatures and then back to the surface through a continuous and closed-loop pipe [92, 10, 107, 70]. Recent studies reveal that working fluid in the closed-loop geothermal system can be water, superheated steam, carbon dioxide, supercritical carbon dioxide, and so on [92, 95, 83]. While the closed-loop system has some disadvantages in the heat exchange efficiency, this system does not lose the working fluid which is isolated from the geothermal reservoir by the closed-loop pipe [92, 95, 107, 70]. Furthermore, for the liquid-dominated hydraulically fractured geothermal reservoir, the closed-loop system does not need to deal with the mixture of the working fluid and the natural fluid, which may erode the well and surface collection pipe [92].

In this paper, we consider the closed-loop system for the geothermal reservoir with porous media flows [70, 34, 35, 99]. On one hand, since the working fluid in the closed-loop pipe does not communicate with the porous media flow in the geothermal reservoir, the traditional Navier/Stokes–Darcy model [41, 42, 62, 77, 96], which was developed to accurately describe the interaction between the fluid flow in the pipe and the porous media flow in the reservoir, is not suitable for the closed-loop geothermal system. On the other hand, even though there is no fluid exchange but only heat exchange between the closed-loop pipe and the geothermal reservoir, both the fluid flow in the pipe and the porous media flow in the reservoir play a key role in the heat transfer of the whole coupled system [70, 99, 89, 34, 106, 3, 45]. Moreover, the geothermal heating system, which consists of a network of underground heat exchange pipelines and pumps to transfer the geothermal heat, has a similar situation. Therefore, there is still a great need to couple the governing PDEs of these physics together in a physically faithful way, which can provide a novel tool to address the effect of the fluid flow in the pipes and the porous media flow in the reservoir on the heat transfer in the whole system.

To the best of our knowledge, there is no such PDE model for the closed-loop geothermal system. Therefore, in this paper we propose a new coupled PDE model for the closed-loop geothermal systems. This model combines the governing equations of the fluid flow in the pipe, the porous media flow in the geothermal reservoir, and the heat flow into a coupled system through the heat exchanging conditions and the no-fluid-communication conditions on the interface between the pipe and porous media. Basically, in the pipe region, the Boussinesq equation, which couples the Navier–Stokes equation and the heat equation, is utilized to govern the fluid flow with heat transfer. In the porous media region, Darcy's law coupled with the heat equation is utilized to govern the porous media flow with heat transfer. Even though the two constitutional models on the two sides of the interface are regular models, the key of an interface model is the appropriate interface conditions to couple the constitutional models. This article is the first one to utilize the heat transfer conditions and no-fluid-communication conditions to couple the two models together for the features of the closed-loop geothermal system. On the interface between the pipe and porous media, four physically valid interface conditions are imposed to ensure the continuity of temperature, the continuity of heat flux, and no-fluid exchange. In addition to the closed-loop geothermal system, the proposed model is also valid for other applications with similar set-up.

The proposed model is a multiphysics interface problem. In the literature, there are many existing methods to solve other types of multiphysics interface problems, such as the interface Poisson/heat/wave equations [7, 32, 46, 68, 67, 69, 79, 103],

interface elasticity problems [57, 80, 81], fluid-fluid interaction [37, 48, 14], Stokes–Darcy model [13, 47, 51, 54, 58, 73, 76, 88, 97], Navier/Stokes–Darcy model [6, 20, 21, 25, 27, 33, 43, 56, 65, 94], and their extensions [84, 16, 29, 31, 40, 52, 64, 74, 100, 104]. These methods can be divided into two main categories, coupled methods [2, 27, 24, 53, 59, 63, 66] and decoupled methods [30, 44, 22, 23, 85, 87].

In this paper, a stabilization term with a penalty parameter is introduced to ensure the stability since the numerical instability occurs due to the interface condition of the heat flux. We first present the basic coupled finite element method which directly arises from the naturally coupled weak formulation of the proposed model. Then, we focus on the development of a decoupled method since it is more cost efficient. A decoupled stabilized finite element method is developed for the spatial discretization, and the backward Euler scheme is utilized for the temporal discretization. In the decoupled scheme, we first decouple the governing equations in the two different flow regions, namely the porous media flow region in the geothermal reservoir and the free flow region in the pipes. Then we decouple the heat equation from the flow equation in each of these two regions. Hence, we finally divide the whole system into four separated equations. The stability of the stabilized decoupled scheme is proved. Four numerical examples are provided to demonstrate the features of the proposed model and numerical method. The first experiment is to show the optimal convergence rate of the proposed method as well as the impact of the penalty parameter on the convergence. The second numerical test is presented to simulate a benchmark problem for thermal convection in a squared cavity. In the third and fourth examples, we study the heat transfer in a simplified closed-loop geothermal system and investigate the effect of different sets of parameters.

This paper is organized as follows. In section 2, the new coupled multiphysics model is proposed. In section 3, the weak formulation, well-posedness, spatial discretization, and the coupled scheme are presented. In section 4, the decoupled stabilized finite element method is proposed and analyzed. In section 5, numerical results are provided. In section 6, a conclusion is drawn.

2. The governing equations. As illustrated in Figure 2.1, the global domain Ω consists of two subdomains, Ω_f and Ω_p, where $\Omega_f,\ \Omega_p \in \mathbb{R}^2$ are open, regular, simply connected, and bounded by Lipschitz continuous boundaries of $\partial\Omega_f \setminus \mathbb{I}$ and $\partial\Omega_p \setminus \mathbb{I}$. Here $\Omega_f \cap \Omega_p = \emptyset$, $\bar{\Omega}_f \cap \bar{\Omega}_p = \mathbb{I}$, and $\bar{\Omega}_f \cup \bar{\Omega}_p = \bar{\Omega}$. $\hat{n}_f$ and $\hat{n}_p$ are the unit normal vectors that point outward from the free flow region Ω_f and porous media flow region Ω_p, respectively. The unit outward normal vectors satisfy the condition of $\hat{n}_p = -\hat{n}_f$ on the interface $\mathbb{I}$. The time frame is considered in $[0, T]$.

In Ω_f, we assume that the fluid flow with heat transfer is governed by the Boussinesq equation, which combines the Navier–Stokes equation with the heat equation [11, 108, 19]:

$$\frac{\partial \vec{u}_f}{\partial t} - \mathrm{Pr}\Delta\vec{u}_f + (\vec{u}_f \cdot \nabla)\vec{u}_f + \nabla p_f = PrRa\vec{\xi}\theta_f + \vec{f}_f \qquad \text{in } \Omega_f \times (0, T], \tag{2.1}$$

$$\nabla \cdot \vec{u}_f = 0 \qquad \text{in } \Omega_f \times (0, T], \tag{2.2}$$

$$\vec{u}_f = 0 \qquad \text{on } \partial\Omega_f \setminus \mathbb{I} \times (0, T], \tag{2.3}$$

$$\vec{u}_f(0, x) = \vec{u}_f^0(x) \qquad \text{in } \Omega_f, \tag{2.4}$$

$$\frac{\partial \theta_f}{\partial t} - k_f\Delta\theta_f + \vec{u}_f \cdot \nabla\theta_f = \Upsilon_f \qquad \text{in } \Omega_f \times (0, T], \tag{2.5}$$

$$\theta_f = 0 \qquad \text{on } \Gamma_M \times (0, T], \tag{2.6}$$

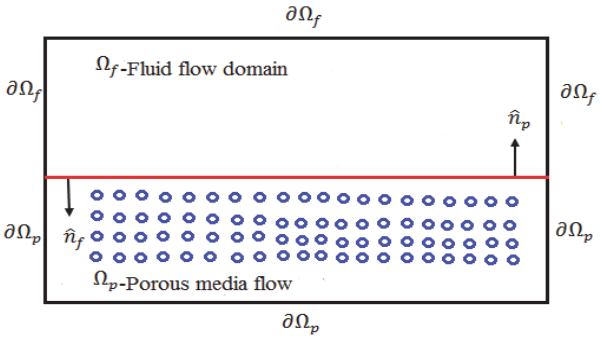

FIG. 2.1. *The global domain Ω consists of free fluid flow subdomain Ω_f and porous media fluid flow subdomain Ω_p, separated by a common interface $\mathbb{I}$.*

$$\frac{\partial \theta_f}{\partial \hat{n}_f} = 0 \qquad \text{on } \Gamma_E \times (0,T], \tag{2.7}$$

$$\theta_f(0,x) = \theta_f^0(x) \qquad \text{in } \Omega_f. \tag{2.8}$$

Here $\vec{u}_f$, p_f, and θ_f denote the free fluid flow region velocity vector field, pressure, and temperature, respectively. The unit vector $\vec{\xi} = [0,1]^T$ denotes the direction of the gravitational acceleration. $\vec{f}_f$ and Υ_f are the external force terms. Pr is the Prandtl number. Ra represents the Rayleigh number, which is the product of Grashof number and Prandtl number. k_f is the nondimensional parameter related to thermal conductivity. Γ_M, Γ_E denote the Dirichlet and the Neumann boundary conditions, respectively, in the pipe region boundaries where $\Gamma_M \cup \Gamma_E = \partial\Omega_f \setminus \mathbb{I}$.

We assume the porous media region Ω_p is homogeneous and isotropic. The porous media flow with heat transfer can be governed by the following Darcy's law coupled with a heat equation:

$$C_a Da \frac{\partial \vec{u}_p}{\partial t} + Pr\vec{u}_p = -Da\nabla\phi_p + PrDaRa\vec{\xi}\theta_p \qquad \text{in } \Omega_p \times (0,T], \tag{2.9}$$

$$\nabla \cdot \vec{u}_p = 0 \qquad \text{in } \Omega_p \times (0,T], \tag{2.10}$$

$$\vec{u}_p(0,x) = \vec{u}_p^0(x) \qquad \text{in } \Omega_p, \tag{2.11}$$

$$\vec{u}_p \cdot \hat{n}_p = 0 \qquad \text{on } \partial\Omega_p \setminus \mathbb{I}, \tag{2.12}$$

$$\frac{\partial \theta_p}{\partial t} - k_p \Delta\theta_p + \vec{u}_p \cdot \nabla\theta_p = \Upsilon_p \qquad \text{in } \Omega_p \times (0,T], \tag{2.13}$$

$$\theta_p = 0 \qquad \text{on } \Gamma_N \times (0,T], \tag{2.14}$$

$$\frac{\partial \theta_p}{\partial \hat{n}_p} = 0 \qquad \text{on } \Gamma_Z \times (0,T], \tag{2.15}$$

$$\theta_p(0,x) = \theta_p^0(x) \qquad \text{in } \Omega_p. \tag{2.16}$$

Here $\vec{u}_p$, ϕ_p, and θ_p denote the porous medium fluid flow region velocity vector field, pressure, and temperature, respectively. The source term is denoted by Υ_p. Da is the Darcy number which represents the relative effect of the permeability of the medium versus the cross-sectional area. C_a is the dimensionless parameter known as acceleration coefficient. k_p denotes the nondimensional parameter related to the thermal conductivity. Γ_N, Γ_Z denote the Dirichlet and Neumann boundary conditions, respectively, in the porous media region boundaries where $\Gamma_N \cup \Gamma_Z = \partial\Omega_p \setminus \mathbb{I}$.

Remark 2.1. The above closed-loop geothermal system (2.1)–(2.16) is presented in a nondimensional form. The dimensional form of the Navier–Stokes equation and Darcy equation with Boussinesq approximation, and heat equation without initial condition, boundary condition and incompressibility condition can be written as [12, 11, 90, 75, 4, 72, 62, 9]:

$$\rho\frac{\partial\tilde{\vec{u}}_f}{\partial\tilde{t}}+\rho(\tilde{\vec{u}}_f\cdot\tilde{\nabla})\tilde{\vec{u}}_f-\mu\tilde{\Delta}\tilde{\vec{u}}_f+\tilde{\nabla}\tilde{p}_f=-\rho g\vec{\xi}\big(1-\beta(\tilde{\theta}_f-\tilde{\theta}_{f,\mathrm{ref}})\big)+\rho\tilde{\vec{f}}_f, \tag{2.17}$$

$$C_a\rho\frac{\partial\tilde{\vec{u}}_p}{\partial\tilde{t}}+\frac{\mu}{k}\tilde{\vec{u}}_p=-\tilde{\nabla}\tilde{\phi}_p-\rho g\vec{\xi}\big(1-\beta(\tilde{\theta}_p-\tilde{\theta}_{p,\mathrm{ref}})\big), \tag{2.18}$$

$$\frac{\partial\tilde{\theta}_\varpi}{\partial\tilde{t}}-\tilde{\alpha}_\varpi\tilde{\Delta}\tilde{\theta}_\varpi+\tilde{\vec{u}}_\varpi\cdot\tilde{\nabla}\tilde{\theta}_\varpi=\tilde{\Upsilon}_\varpi, \tag{2.19}$$

where $\varpi=f$ or p represent the fluid domain and porous media domain, respectively. μ, k, g, and β are the dynamic viscosity, permeability, acceleration due to gravity, and thermal expansion coefficient, respectively. $\tilde{\theta}_{f,\mathrm{ref}}$ and $\tilde{\theta}_{p,\mathrm{ref}}$ are the reference or fixed temperature. Thermal diffusivity is represented by $\tilde{\alpha}_\varpi=\frac{\tilde{k}_\varpi}{\rho C_{p\varpi}}$, where $C_{p\varpi}$ is the specific heat, ρ is the density of fluid, and $\tilde{k}_\varpi$ is the thermal conductivity. To nondimensionalize the closed-loop geothermal system [12, 93, 49, 28], we introduce the nondimensional variables by choosing $\tilde{x}=Lx$, $\tilde{\vec{u}}_\varpi=\frac{\alpha_\varpi}{L}\vec{u}_\varpi$, $\tilde{t}=\frac{L^2}{\alpha_\varpi}t$, $\tilde{p}_f=\frac{\rho\alpha_f^2}{L^2}p_f$, $\tilde{\phi}_p=\frac{\rho\alpha_p^2}{L^2}\phi_p$, $\tilde{\theta}_\varpi=(\theta_{\varpi,H}-\theta_{\varpi,c})\theta_\varpi+\theta_{\varpi,c}$, $\tilde{\vec{f}}_f=\frac{\alpha_f^2}{L^3}\vec{f}_f$, $\tilde{\Upsilon}_\varpi=\frac{\alpha_\varpi(\theta_{\varpi,H}-\theta_{\varpi,c})}{L^2}\Upsilon_\varpi$, $Ra=\frac{\beta L^3 g(\theta_{\varpi,H}-\theta_{\varpi,c})}{\nu\alpha_\varpi}$, $Pr=\frac{\nu}{\alpha_\varpi}$, $Da=\frac{k}{L^2}$, and $\tilde{\alpha}_\varpi=\alpha_\varpi k_\varpi$. Here L represents the characteristics length, ν represents the kinematic viscosity, $\theta_{\varpi,H}$ represents the hot wall, and $\theta_{\varpi,c}$ represents the cold wall. By plugging the above nondimensional variables into (2.17)–(2.19), one can easily derive the closed-loop geothermal system (2.1)–(2.16). Moreover, the units of the variables and parameters can be defined as $\rho=kgm^{-3}$, $\tilde{\vec{u}}_\varpi=ms^{-1}$, $\tilde{\theta}_\varpi=K$, $\tilde{\theta}_{\varpi,\mathrm{ref}}=K$, $\tilde{p}_f=Pa$ or $kgm^{-1}s^{-2}$, $\tilde{\phi}_p=Pa$ or $kgm^{-1}s^{-2}$, $\mu=Pa\cdot s$ or $kgm^{-1}s^{-1}$, $\nu=m^2s^{-1}$, $\beta=K^{-1}$, $\tilde{\alpha}_\varpi=m^2s^{-1}$, $g=ms^{-2}$, and $k=m^2$. The units of the terms in (2.17)–(2.19) can be verified to be consistent by plugging the above units into the equations.

Since the closed-loop system does not have fluid communication but only heat transfer between the reservoir and the pipe, we use the following two heat exchanging interface conditions and two no-fluid-communication conditions on the interface $\mathbb{I}$ [91, 18, 72, 60].

- Continuity of temperature across the interface:

$$\theta_f=\theta_p \qquad \text{on } \mathbb{I}. \tag{2.20}$$

- Continuity of heat flux across the interface:

$$\hat{n}_f\cdot k_f\nabla\theta_f=-\hat{n}_p\cdot k_p\nabla\theta_p \qquad \text{on } \mathbb{I}. \tag{2.21}$$

- No-communication and no-slip conditions for the free flow on the interface:

$$\vec{u}_f\cdot\hat{n}_f=0, \qquad \vec{u}_f\cdot\vec{\tau}=0 \qquad \text{on } \mathbb{I}, \tag{2.22}$$

  where $\vec{\tau}$ denotes the unit tangential vector along the interface.
- No-porous media flow passing through the interface:

$$\vec{u}_p\cdot\hat{n}_p=0 \qquad \text{on } \mathbb{I}. \tag{2.23}$$

3. Preliminaries, variational formulation, and the coupled discretization scheme. We use standard notation throughout the paper for Lebesgue and Sobolev spaces. The inner product in $L^2(D)$ is associated with $(\cdot,\cdot)$ and the norm of $L^2(D)$ is denoted by $\|\cdot\|_{L^2(D)}$, where D may be Ω_f, Ω_p, or $\mathbb{I}$.

In order to derive the variational formulation for the model problem (2.1) to (2.23), we define the following spaces:

$$
\begin{aligned}
Y_f &:= H_0^1(\Omega_f)^2 := \{\vec{v}_f \in H^1(\Omega_f)^2 : \vec{v}_f = 0 \ \text{ on } \ \partial\Omega_f\},\\
Y_p &:= H(\mathrm{div};\Omega_p) := \{\vec{v}_p \in L^2(\Omega_p)^2, \nabla\cdot\vec{v}_p \in L^2(\Omega_p) : \vec{v}_p\cdot\hat{n}_p = 0 \ \text{ on } \ \partial\Omega_p\},\\
T_f &:= H_0^1(\Omega_f) := \{\varphi \in H^1(\Omega_f) : \varphi = 0 \ \text{ on } \ \Gamma_M\},\\
T_p &:= H_0^1(\Omega_p) := \{\omega \in H^1(\Omega_p) : \omega = 0 \ \text{ on } \ \Gamma_N\},\\
Q_f &:= L_0^2(\Omega_f) := \left\{q \in L^2(\Omega_f) : \int_{\Omega_f} q dx = 0\right\},\\
Q_p &:= L_0^2(\Omega_p) := \left\{\psi \in L^2(\Omega_p) : \int_{\Omega_p} \psi dx = 0\right\}.
\end{aligned}
$$

Define a product space

$$W_T = T_f \times T_p, \tag{3.1}$$

and

$$W_{\mathbb{I}} := \{(\varphi,\omega) \in (T_f \times T_p) : \varphi|_{\mathbb{I}} = \omega|_{\mathbb{I}}\} \subset W_T.$$

We also define the solenoidal spaces

$$V_f := \{\vec{v}_f \in Y_f : \nabla\cdot\vec{v}_f = 0\} \quad \text{and} \quad V_p := \{\vec{v}_p \in Y_p : \nabla\cdot\vec{v}_p = 0\}.$$

The trilinear form is defined as follows:

$$
\begin{aligned}
c^{\mathrm{tri}}(\vec{u}_f,\vec{v}_f,\vec{w})_{\Omega_f} &= ((\vec{u}_f\cdot\nabla)\vec{v}_f,\vec{w})_{\Omega_f} + \frac{1}{2}((\mathrm{div}\vec{u}_f)\vec{v}_f,\vec{w})_{\Omega_f}\\
&= \frac{1}{2}((\vec{u}_f\cdot\nabla)\vec{v}_f,\vec{w})_{\Omega_f} - \frac{1}{2}((\vec{u}_f\cdot\nabla)\vec{w},\vec{v}_f)_{\Omega_f} \quad \forall\, \vec{u}_f,\vec{v}_f,\vec{w} \in Y_f.
\end{aligned} \tag{3.2}
$$

In a similar manner, we define another two trilinear forms for any $(\varphi,\omega) \in W_{\mathbb{I}}$ and $(\theta_f,\theta_p) \in W_T$:

$$
\begin{aligned}
t_f^{\mathrm{tri}}(\vec{u}_f,\theta_f,\varphi)_{\Omega_f} &= \frac{1}{2}((\vec{u}_f\cdot\nabla)\theta_f,\varphi)_{\Omega_f} - \frac{1}{2}((\vec{u}_f\cdot\nabla)\varphi,\theta_f)_{\Omega_f} \quad \forall\, \vec{u}_f \in Y_f,\\
t_p^{\mathrm{tri}}(\vec{u}_p,\theta_p,\omega)_{\Omega_p} &= \frac{1}{2}((\vec{u}_p\cdot\nabla)\theta_p,\omega)_{\Omega_p} - \frac{1}{2}((\vec{u}_p\cdot\nabla)\omega,\theta_p)_{\Omega_p} \quad \forall\, \vec{u}_p \in Y_p.
\end{aligned} \tag{3.3}
$$

Moreover, if $\vec{u}_f \in V_f$ and $\vec{u}_p \in V_p$, then for any $(\vec{v}_f,\vec{w}) \in Y_f$, $(\theta_f,\theta_p) \in W_T$, and $(\varphi,\omega) \in W_{\mathbb{I}}$, we have [36]

$$
\begin{aligned}
&c^{\mathrm{tri}}(\vec{u}_f,\vec{v}_f,\vec{w})_{\Omega_f} = ((\vec{u}_f\cdot\nabla)\vec{v}_f,\vec{w})_{\Omega_f},\ t_f^{\mathrm{tri}}(\vec{u}_f,\theta_f,\varphi)_{\Omega_f} = ((\vec{u}_f\cdot\nabla)\theta_f,\varphi)_{\Omega_f},\\
&t_p^{\mathrm{tri}}(\vec{u}_p,\theta_p,\omega)_{\Omega_p} = ((\vec{u}_p\cdot\nabla)\theta_p,\omega)_{\Omega_p}.
\end{aligned}
$$

The weak formulations of the coupled system (2.1)–(2.23) are to find $(\vec{u}_f,\vec{u}_p;p_f,\phi_p;\theta_f,\theta_p) \in (Y_f \times Y_p \times Q_f \times Q_p \times W_T)$ such that for any $(\vec{v}_f,\vec{v}_p;q,\psi;\varphi,\omega) \in (Y_f \times Y_p \times Q_f \times Q_p \times W_{\mathbb{I}})$,

$$\left(\frac{\partial\vec{u}_f}{\partial t},\vec{v}_f\right)_{\Omega_f} + C_a Da\left(\frac{\partial\vec{u}_p}{\partial t},\vec{v}_p\right)_{\Omega_p} - (p_f,\nabla\cdot\vec{v}_f)_{\Omega_f} + Pr(\nabla\vec{u}_f,\nabla\vec{v}_f)_{\Omega_f}$$

$$+c^{\mathrm{tri}}(\vec{u}_f,\vec{u}_f,\vec{v}_f)_{\Omega_f}+Pr(\vec{u}_p,\vec{v}_p)_{\Omega_p}-Da(\phi_p,\nabla\cdot\vec{v}_p)_{\Omega_p}$$

$$=PrRa(\vec{\xi}\theta_f,\vec{v}_f)_{\Omega_f}+PrDaRa(\vec{\xi}\theta_p,\vec{v}_p)_{\Omega_p}+(\vec{f}_f,\vec{v}_f)_{\Omega_f}, \tag{3.4}$$

$$(q,\nabla\cdot\vec{u}_f)_{\Omega_f}=0, \tag{3.5}$$

$$Da(\psi,\nabla\cdot\vec{u}_p)_{\Omega_p}=0, \tag{3.6}$$

$$\left(\frac{\partial\theta_f}{\partial t},\varphi\right)_{\Omega_f}+\left(\frac{\partial\theta_p}{\partial t},\omega\right)_{\Omega_p}+k_f(\nabla\theta_f,\nabla\varphi)_{\Omega_f}+k_p(\nabla\theta_p,\nabla\omega)_{\Omega_p}$$

$$+t_f^{\mathrm{tri}}(\vec{u}_f,\theta_f,\varphi)_{\Omega_f}+t_p^{\mathrm{tri}}(\vec{u}_p,\theta_p,\omega)_{\Omega_p}-k_f\int_{\mathbb{I}}\hat{n}_f\cdot\nabla\theta_f(\varphi-\omega)dl$$

$$+\frac{k_f\gamma}{h}\int_{\mathbb{I}}(\theta_f-\theta_p)(\varphi-\omega)dl=(\Upsilon_f,\varphi)_{\Omega_f}+(\Upsilon_p,\omega)_{\Omega_p}. \tag{3.7}$$

Based on the divergence-free space [12, 26, 25, 8, 101, 55], we construct the equivalent formulation of the weak form (3.4)–(3.7) for the analysis below. To find $(\vec{u}_f,\vec{u}_p;\theta_f,\theta_p)\in(V_f\times V_p\times W_T)$ such that for any $(\vec{v}_f,\vec{v}_p;\varphi,\omega)\in(V_f\times V_p\times W_{\mathbb{I}})$, we can obtain

$$\begin{aligned}&\left(\frac{\partial\vec{u}_f}{\partial t},\vec{v}_f\right)_{\Omega_f}+C_aDa\left(\frac{\partial\vec{u}_p}{\partial t},\vec{v}_p\right)_{\Omega_p}+Pr(\nabla\vec{u}_f,\nabla\vec{v}_f)_{\Omega_f}\\&\quad+((\vec{u}_f\cdot\nabla)\vec{u}_f,\vec{v}_f)_{\Omega_f}+Pr(\vec{u}_p,\vec{v}_p)_{\Omega_p}\\&\quad=PrRa(\vec{\xi}\theta_f,\vec{v}_f)_{\Omega_f}+PrDaRa(\vec{\xi}\theta_p,\vec{v}_p)_{\Omega_p}+(\vec{f}_f,\vec{v}_f)_{\Omega_f},\end{aligned} \tag{3.8}$$

$$\begin{aligned}&\left(\frac{\partial\theta_f}{\partial t},\varphi\right)_{\Omega_f}+\left(\frac{\partial\theta_p}{\partial t},\omega\right)_{\Omega_p}+k_f(\nabla\theta_f,\nabla\varphi)_{\Omega_f}+k_p(\nabla\theta_p,\nabla\omega)_{\Omega_p}\\&+((\vec{u}_f\cdot\nabla)\theta_f,\varphi)_{\Omega_f}+((\vec{u}_p\cdot\nabla)\theta_p,\omega)_{\Omega_p}-k_f\int_{\mathbb{I}}\hat{n}_f\cdot\nabla\theta_f(\varphi-\omega)dl\\&+\frac{k_f\gamma}{h}\int_{\mathbb{I}}(\theta_f-\theta_p)(\varphi-\omega)dl=(\Upsilon_f,\varphi)_{\Omega_f}+(\Upsilon_p,\omega)_{\Omega_p}.\end{aligned} \tag{3.9}$$

Remark 3.1. The interface conditions utilized in the proposed model belong to the range of Nitsche's interface, which is well-known for the possibility to cause numerical instability [91, 61]. The artificial energy transfers induced by the interface decoupling are believed to be the main reason for the numerical instability [48, 18]. Particularly, in the variational formulation (3.7), $-k_f\int_{\mathbb{I}}\hat{n}_f\cdot\nabla\theta_f(\varphi-\omega)dl$ arises from the interface condition (2.21) and its approximation causes the instability due to the difficulty in controlling the interface terms $\|\nabla\theta_f\|_{L^2(\mathbb{I})}$ and $\|\varphi-\omega\|_{L^2(\mathbb{I})}$. To overcome this difficulty, we introduce a stabilization term $\frac{k_f\gamma}{h}\int_{\mathbb{I}}(\theta_f-\theta_p)(\varphi-\omega)dl$, which does not affect the consistency of the formulation due to the interface condition (2.20) but ensures the stability of the finite element schemes. The penalty parameter γ is dimensionless and should be chosen to be positive to ensure the coercivity. Besides, we assume h is constant in the variational formulation while it represents the mesh size in the finite element schemes. The importance of the stabilization term and the penalty parameter will be also numerically illustrated in section 5.1.

Remark 3.2. The interface term $k_f\int_{\mathbb{I}}\hat{n}_f\cdot\nabla\theta_f(\varphi-\omega)dl$ and the stabilization term $\frac{k_f\gamma}{h}\int_{\mathbb{I}}(\theta_f-\theta_p)(\varphi-\omega)dl$ of the weak formulation (3.7) vanish when the coupled space $W_{\mathbb{I}}$ is applied. Hence, the well-posedness of the system is classic. Moreover, we will propose the finite element schemes by splitting the tensor spaces $W_{\mathbb{I}}$ and W_T.

LEMMA 3.1 (see [50]). *If $\vec{u}_f \in Y_f$, then there exists a positive constant $C > 0$ such that*

$$\|\vec{u}_f\|_{L^4(\Omega_f)} \le C\|\vec{u}_f\|^{1/2}_{L^2(\Omega_f)}\|\nabla\vec{u}_f\|^{1/2}_{L^2(\Omega_f)}. \tag{3.10}$$

THEOREM 3.2 (well-posedness). *The weak formulation of the closed-loop geothermal system* (3.4)–(3.7) *has a unique weak solution* $(\vec{u}_f, \vec{u}_p; p_f, \phi_p; \theta_f, \theta_p) \in (Y_f \times Y_p \times Q_f \times Q_p \times W_T)$ *satisfying*

$$\begin{aligned}
&\vec{u}_f \in L^\infty(0,T;L^2(\Omega_f)) \cap L^2(0,T;Y_f), \quad \vec{u}_p \in L^\infty(0,T;L^2(\Omega_p)) \cap L^2(0,T;L^2(\Omega_p)),\\
&p_f \in L^2(0,T;Q_f), \phi_p \in L^2(0,T;Q_p), \quad \theta_f \in L^\infty(0,T;L^2(\Omega_f)) \cap L^2(0,T;T_f),\\
&\theta_p \in L^\infty(0,T;L^2(\Omega_p)) \cap L^2(0,T;T_p).
\end{aligned}$$

Proof. The interface term $k_f \int_{\mathbb{I}} \hat{n}_f \cdot \nabla\theta_f(\varphi - \omega)dl$ and the stabilization term $\frac{k_f\gamma}{h}\int_{\mathbb{I}}(\theta_f - \theta_p)(\varphi - \omega)dl$ of the weak formulation (3.7) vanish when the coupled space $W_{\mathbb{I}}$ is applied. Since the other parts of the weak formulation (3.4)–(3.7) are the regular components in the traditional Boussinesq equation, Darcy's law coupled with heat equation, and interface heat transfer problem, the existence of the weak formulation (3.4)–(3.7) can be obtained by following and combining the classic procedures for the well-posedness of similar problems [26, 25, 37, 36, 8, 101, 78, 39, 11]. We omit the details here due to page limitation.

To prove the uniqueness of the weak formulation (3.4)–(3.7), we assume there exist two solutions:

$$(\vec{u}_f^1, \vec{u}_p^1; p_f^1, \phi_p^1; \theta_f^1, \theta_p^1) \quad \text{and} \quad (\vec{u}_f^2, \vec{u}_p^2; p_f^2, \phi_p^2; \theta_f^2, \theta_p^2).$$

We define the differences between them as follows:

$$\begin{aligned}
&\vec{u}_f^1 - \vec{u}_f^2 = \mathbf{e}_{\vec{u}_f}, \quad p_f^1 - p_f^2 = e_{p_f}, \quad \theta_f^1 - \theta_f^2 = e_{\theta_f},\\
&\vec{u}_p^1 - \vec{u}_p^2 = \mathbf{e}_{\vec{u}_p}, \quad \phi_p^1 - \phi_p^2 = e_{\phi_p}, \quad \theta_p^1 - \theta_p^2 = e_{\theta_p}.
\end{aligned}$$

To prove the uniqueness of (3.4)–(3.7), we choose the test functions $\vec{v}_f = \mathbf{e}_{\vec{u}_f}$, $\vec{v}_p = \mathbf{e}_{\vec{u}_p}$, $\varphi = e_{\theta_f}$, and $\omega = e_{\theta_p}$ in (3.8)–(3.9). Again, the interface term $k_f \int_{\mathbb{I}} \hat{n}_f \cdot \nabla\theta_f(\varphi - \omega)dl$ and the stabilization term $\frac{k_f\gamma}{h}\int_{\mathbb{I}}(\theta_f - \theta_p)(\varphi - \omega)dl$ of the weak formulation (3.9) vanish when the coupled space $W_{\mathbb{I}}$ is applied. Since both of the two solutions satisfy (3.8) and (3.9), then by taking the subtraction between the two sets of equations of the two solutions, we can obtain

$$\begin{aligned}
&\frac{1}{2}\frac{d}{dt}\|\mathbf{e}_{\vec{u}_f}\|^2_{L^2(\Omega_f)} + \frac{C_aDa}{2}\frac{d}{dt}\|\mathbf{e}_{\vec{u}_p}\|^2_{L^2(\Omega_p)} + Pr\|\nabla\mathbf{e}_{\vec{u}_f}\|^2_{L^2(\Omega_f)}\\
&\quad + Pr\|\mathbf{e}_{\vec{u}_p}\|^2_{L^2(\Omega_p)} + (\mathbf{e}_{\vec{u}_f} \cdot \nabla\vec{u}_f^1, \mathbf{e}_{\vec{u}_f})_{\Omega_f}\\
&\quad + (\vec{u}_f^2 \cdot \nabla\mathbf{e}_{\vec{u}_f}, \mathbf{e}_{\vec{u}_f})_{\Omega_f} = PrRa(\vec{\xi}e_{\theta_f}, \mathbf{e}_{\vec{u}_f})_{\Omega_f} + PrDaRa(\vec{\xi}e_{\theta_p}, \mathbf{e}_{\vec{u}_p})_{\Omega_p},
\end{aligned} \tag{3.11}$$

$$\begin{aligned}
&\frac{1}{2}\frac{d}{dt}\|e_{\theta_f}\|^2_{L^2(\Omega_f)} + \frac{1}{2}\frac{d}{dt}\|e_{\theta_p}\|^2_{L^2(\Omega_p)} + k_f\|\nabla e_{\theta_f}\|^2_{L^2(\Omega_f)}\\
&\quad + k_p\|\nabla e_{\theta_p}\|^2_{L^2(\Omega_p)} + (\mathbf{e}_{\vec{u}_f} \cdot \nabla\theta_f^1, e_{\theta_f})_{\Omega_f}\\
&\quad + (\vec{u}_f^2 \cdot \nabla e_{\theta_f}, e_{\theta_f})_{\Omega_f} + (\mathbf{e}_{\vec{u}_p} \cdot \nabla\theta_p^1, e_{\theta_p})_{\Omega_p} + (\vec{u}_p^2 \cdot \nabla e_{\theta_p}, e_{\theta_p})_{\Omega_p} = 0.
\end{aligned} \tag{3.12}$$

Since $(\vec{u}_f^2 \cdot \nabla \mathbf{e}_{\vec{u}_f}, \mathbf{e}_{\vec{u}_f})_{\Omega_f}$, $(\vec{u}_f^2 \cdot \nabla e_{\theta_f}, e_{\theta_f})_{\Omega_f}$, and $(\vec{u}_p^2 \cdot \nabla e_{\theta_p}, e_{\theta_p})_{\Omega_p}$ are equal to zero, then we can obtain

(3.13)
$$\begin{aligned}
&\frac{d}{dt}\Big(\|\mathbf{e}_{\vec{u}_f}\|^2_{L^2(\Omega_f)} + C_a Da\|\mathbf{e}_{\vec{u}_p}\|^2_{L^2(\Omega_p)} + \|e_{\theta_f}\|^2_{L^2(\Omega_f)} + \|e_{\theta_p}\|^2_{L^2(\Omega_p)}\Big)\\
&+ 2\Big(Pr\|\nabla \mathbf{e}_{\vec{u}_f}\|^2_{L^2(\Omega_f)} + Pr\|\mathbf{e}_{\vec{u}_p}\|^2_{L^2(\Omega_p)} + k_f\|\nabla e_{\theta_f}\|^2_{L^2(\Omega_f)} + k_p\|\nabla e_{\theta_p}\|^2_{L^2(\Omega_p)}\Big)\\
&\qquad \le \big|2PrRa(\vec{\xi} e_{\theta_f}, \mathbf{e}_{\vec{u}_f})_{\Omega_f}\big| + \big|2PrDaRa(\vec{\xi} e_{\theta_p}, \mathbf{e}_{\vec{u}_p})_{\Omega_p}\big| + \big|2(\mathbf{e}_{\vec{u}_f} \cdot \nabla \vec{u}_f^1, \mathbf{e}_{\vec{u}_f})_{\Omega_f}\big|\\
&\qquad + \big|2(\mathbf{e}_{\vec{u}_f} \cdot \nabla \theta_f^1, e_{\theta_f})_{\Omega_f}\big| + \big|2(\mathbf{e}_{\vec{u}_p} \cdot \nabla \theta_p^1, e_{\theta_p})_{\Omega_p}\big|.
\end{aligned}$$

In the following, we will estimate the terms on the right-hand side of (3.13) one by one as follows. First, we have

$$\big|2PrRa(\vec{\xi} e_{\theta_f}, \mathbf{e}_{\vec{u}_f})_{\Omega_f}\big| \le C_{(Pr,Ra)}\Big(\|e_{\theta_f}\|^2_{L^2(\Omega_f)} + \|\mathbf{e}_{\vec{u}_f}\|^2_{L^2(\Omega_f)}\Big), \tag{3.14}$$

$$\big|2PrDaRa(\vec{\xi} e_{\theta_p}, \mathbf{e}_{\vec{u}_p})_{\Omega_p}\big| \le C_{(Pr,Da,Ra)}\|e_{\theta_p}\|^2_{L^2(\Omega_p)} + Pr\|\mathbf{e}_{\vec{u}_p}\|^2_{L^2(\Omega_p)}. \tag{3.15}$$

Then we estimate the nonlinear convective terms

$$\begin{aligned}
\Big|2(\mathbf{e}_{\vec{u}_f} \cdot \nabla \vec{u}_f^1, \mathbf{e}_{\vec{u}_f})_{\Omega_f}\Big| &\le 2\|\mathbf{e}_{\vec{u}_f}\|^2_{L^4(\Omega_f)}\|\nabla \vec{u}_f^1\|_{L^2(\Omega_f)}\\
&\le 2C\|\mathbf{e}_{\vec{u}_f}\|_{L^2(\Omega_f)}\|\nabla \mathbf{e}_{\vec{u}_f}\|_{L^2(\Omega_f)}\|\nabla \vec{u}_f^1\|_{L^2(\Omega_f)}\\
&\le C_{Pr}\|\mathbf{e}_{\vec{u}_f}\|^2_{L^2(\Omega_f)}\|\nabla \vec{u}_f^1\|^2_{L^2(\Omega_f)} + \frac{Pr}{2}\|\nabla \mathbf{e}_{\vec{u}_f}\|^2_{L^2(\Omega_f)}.
\end{aligned} \tag{3.16}$$

Similarly, we can obtain

$$\begin{aligned}
&\Big|2(\mathbf{e}_{\vec{u}_f} \cdot \nabla \theta_f^1, e_{\theta_f})_{\Omega_f}\Big|\\
&\quad \le 2\|\mathbf{e}_{\vec{u}_f}\|_{L^4(\Omega_f)}\|\nabla \theta_f^1\|_{L^2(\Omega_f)}\|e_{\theta_f}\|_{L^4(\Omega_f)}\\
&\quad \le 2C\|\mathbf{e}_{\vec{u}_f}\|^{1/2}_{L^2(\Omega_f)}\|\nabla \mathbf{e}_{\vec{u}_f}\|^{1/2}_{L^2(\Omega_f)}\|\nabla \theta_f^1\|^{1/2}_{L^2(\Omega_f)}\|\nabla \theta_f^1\|^{1/2}_{L^2(\Omega_f)}\|e_{\theta_f}\|^{1/2}_{L^2(\Omega_f)}\|\nabla e_{\theta_f}\|^{1/2}_{L^2(\Omega_f)}\\
&\quad = \frac{2C}{(k_f Pr)^{1/4}}\|\mathbf{e}_{\vec{u}_f}\|^{1/2}_{L^2(\Omega_f)}\|\nabla \theta_f^1\|^{1/2}_{L^2(\Omega_f)}\|e_{\theta_f}\|^{1/2}_{L^2(\Omega_f)}\|\nabla \theta_f^1\|^{1/2}_{L^2(\Omega_f)}(k_f Pr)^{1/4}\\
&\quad \cdot \|\nabla \mathbf{e}_{\vec{u}_f}\|^{1/2}_{L^2(\Omega_f)}\|\nabla e_{\theta_f}\|^{1/2}_{L^2(\Omega_f)}\\
&\quad \le \frac{C^2}{(k_f Pr)^{1/2}}\|\mathbf{e}_{\vec{u}_f}\|_{L^2(\Omega_f)}\|\nabla \theta_f^1\|_{L^2(\Omega_f)}\|e_{\theta_f}\|_{L^2(\Omega_f)}\|\nabla \theta_f^1\|_{L^2(\Omega_f)}\\
&\quad + (k_f Pr)^{1/2}\|\nabla \mathbf{e}_{\vec{u}_f}\|_{L^2(\Omega_f)}\|\nabla e_{\theta_f}\|_{L^2(\Omega_f)}\\
&\quad \le C_{(k_f,Pr)}\Big(\|\mathbf{e}_{\vec{u}_f}\|^2_{L^2(\Omega_f)}\|\nabla \theta_f^1\|^2_{L^2(\Omega_f)} + \|e_{\theta_f}\|^2_{L^2(\Omega_f)}\|\nabla \theta_f^1\|^2_{L^2(\Omega_f)}\Big)\\
&\qquad + \Big(\frac{k_f}{2}\|\nabla e_{\theta_f}\|^2_{L^2(\Omega_f)} + \frac{Pr}{2}\|\nabla \mathbf{e}_{\vec{u}_f}\|^2_{L^2(\Omega_f)}\Big)
\end{aligned} \tag{3.17}$$

and

$$\begin{aligned}
\Big|2(\mathbf{e}_{\vec{u}_p} \cdot \nabla \theta_p^1, e_{\theta_p})_{\Omega_p}\Big| &= \Big|2(\mathbf{e}_{\vec{u}_p} \cdot \nabla e_{\theta_p}, \theta_p^1)_{\Omega_p}\Big|\\
&\le 2C\|\mathbf{e}_{\vec{u}_p}\|_{L^2(\Omega_p)}\|\theta_p^1\|_{L^\infty(\Omega_p)}\|\nabla e_{\theta_p}\|_{L^2(\Omega_p)}
\end{aligned}$$

$$\leq C_{k_p}\|\mathbf{e}_{\vec{u}_p}\|^2_{L^2(\Omega_p)}\|\theta^1_p\|^2_{L^\infty(\Omega_p)} + \frac{k_p}{2}\|\nabla e_{\theta_p}\|^2_{L^2(\Omega_p)}. \tag{3.18}$$

Here $\theta^1_p \in L^\infty(\Omega_p)$ [8].

Plugging the above estimates into (3.13), we can obtain

$$\begin{aligned}
&\frac{d}{dt}\Big(\|\mathbf{e}_{\vec{u}_f}\|^2_{L^2(\Omega_f)} + C_a Da\|\mathbf{e}_{\vec{u}_p}\|^2_{L^2(\Omega_p)} + \|e_{\theta_f}\|^2_{L^2(\Omega_f)} + \|e_{\theta_p}\|^2_{L^2(\Omega_p)}\Big)\\
&+ \Big(Pr\|\nabla\mathbf{e}_{\vec{u}_f}\|^2_{L^2(\Omega_f)} + Pr\|\mathbf{e}_{\vec{u}_p}\|^2_{L^2(\Omega_p)}\\
&+ \frac{3k_f}{2}\|\nabla e_{\theta_f}\|^2_{L^2(\Omega_f)} + \frac{3k_p}{2}\|\nabla e_{\theta_p}\|^2_{L^2(\Omega_p)}\Big)\\
&\leq M(t)\Big\{\|\mathbf{e}_{\vec{u}_f}\|^2_{L^2(\Omega_f)} + \|e_{\theta_f}\|^2_{L^2(\Omega_f)} + \|e_{\theta_p}\|^2_{L^2(\Omega_p)}\Big\},
\end{aligned} \tag{3.19}$$

where $M(t) = C_{(Pr,Ra,Da,k_f,k_p)}\big\{1 + \|\nabla\vec{u}^1_f\|^2_{L^2(\Omega_f)} + \|\nabla\theta^1_f\|^2_{L^2(\Omega_f)} + \|\theta^1_p\|^2_{L^\infty(\Omega_p)}\big\}$. Integrating (3.19) in time and using the Gronwall inequality can lead to

$$\begin{aligned}
&\Big\{\|\mathbf{e}_{\vec{u}_f}(t)\|^2_{L^2(\Omega_f)} + C_a Da\|\mathbf{e}_{\vec{u}_p}(t)\|^2_{L^2(\Omega_p)} + \|e_{\theta_f}(t)\|^2_{L^2(\Omega_f)} + \|e_{\theta_p}(t)\|^2_{L^2(\Omega_p)}\Big\}\\
&+ \int_0^t \Big(Pr\|\nabla\mathbf{e}_{\vec{u}_f}(s)\|^2_{L^2(\Omega_f)} + Pr\|\mathbf{e}_{\vec{u}_p}(s)\|^2_{L^2(\Omega_p)} + \frac{3k_f}{2}\|\nabla e_{\theta_f}(s)\|^2_{L^2(\Omega_f)}\\
&+ \frac{3k_p}{2}\|\nabla e_{\theta_p}(s)\|^2_{L^2(\Omega_p)}\Big)ds \leq \exp\Big(\int_0^t M(s)ds\Big)\Big\{\|\mathbf{e}_{\vec{u}_f}(0)\|^2_{L^2(\Omega_f)}\\
&+ C_a Da\|\mathbf{e}_{\vec{u}_p}(0)\|^2_{L^2(\Omega_p)} + \|e_{\theta_f}(0)\|^2_{L^2(\Omega_f)} + \|e_{\theta_p}(0)\|^2_{L^2(\Omega_p)}\Big\}.
\end{aligned} \tag{3.20}$$

Since the four solutions satisfy the initial conditions, then $\mathbf{e}_{\vec{u}_f}(0) = 0$, $\mathbf{e}_{\vec{u}_p}(0) = 0$, $e_{\theta_f}(0) = 0$, and $e_{\theta_p}(0) = 0$. Hence

$$\begin{aligned}
&\Big\{\|\mathbf{e}_{\vec{u}_f}(t)\|^2_{L^2(\Omega_f)} + C_a Da\|\mathbf{e}_{\vec{u}_p}(t)\|^2_{L^2(\Omega_p)} + \|e_{\theta_f}(t)\|^2_{L^2(\Omega_f)} + \|e_{\theta_p}(t)\|^2_{L^2(\Omega_p)}\Big\}\\
&+ \int_0^t \Big(Pr\|\nabla\mathbf{e}_{\vec{u}_f}(s)\|^2_{L^2(\Omega_f)} + Pr\|\mathbf{e}_{\vec{u}_p}(s)\|^2_{L^2(\Omega_p)} + \frac{3k_f}{2}\|\nabla e_{\theta_f}(s)\|^2_{L^2(\Omega_f)}\\
&+ \frac{3k_p}{2}\|\nabla e_{\theta_p}(s)\|^2_{L^2(\Omega_p)}\Big)ds \leq 0,
\end{aligned} \tag{3.21}$$

which shows that $\mathbf{e}_{\vec{u}_f}(t) = 0$, $\mathbf{e}_{\vec{u}_p}(t) = 0$, $e_{\theta_f}(t) = 0$, and $e_{\theta_p}(t) = 0$ for $t \in [0, T]$. Plugging these results back into the weak formulation, we obtain

$$(e_{p_f}, \nabla\cdot\vec{v}_f)_{\Omega_f} = 0, \tag{3.22}$$

$$Da(e_{\phi_p}, \nabla\cdot\vec{v}_p)_{\Omega_p} = 0. \tag{3.23}$$

Hence, the uniqueness of the weak formulation (3.4)–(3.7) of the geothermal system can be proved. ∎

LEMMA 3.3 (discrete Gronwall's lemma). *Let C and a_k, b_k, c_k, d_k for integer $k \geq 0$ be nonnegative numbers such that* [71, 98]

$$a_n + \Delta t\sum_{k=0}^n b_k \leq \Delta t\sum_{k=0}^n d_k a_k + \Delta t\sum_{k=0}^n c_k + C \quad \forall\, n \geq 1.$$

Suppose that $\Delta t d_k \leq 1$ for all k; then we have

$$a_n + \Delta t\sum_{k=0}^n b_k \leq \exp\Big(\Delta t\sum_{k=0}^n d_k\Big)\Big(\Delta t\sum_{k=0}^n c_k + C\Big) \quad \forall\, n \geq 1. \tag{3.24}$$

From the trace inequality, there exists a positive constant C_T depending on the domain Ω_f such that for all $\varphi \in T_f$ [102, 1],

$$\|\varphi\|_{L^2(\mathbb{I})} \le C_T \|\varphi\|^{1/2}_{L^2(\Omega_f)} \|\nabla\varphi\|^{1/2}_{L^2(\Omega_f)}. \tag{3.25}$$

From now on, we assume the shapes of Ω_f, Ω_p, and Ω are polygons or polyhedrons. Let $\mathcal{T}_f^h$ and $\mathcal{T}_p^h$ denote the uniformly regular triangulations of Ω_f and Ω_p, respectively, where $h > 0$ is the mesh size. We consider that the two meshes coincide on the interface $\mathbb{I}$ such that $\mathcal{T}^h := \mathcal{T}_f^h \cup \mathcal{T}_p^h$ is the triangulations of $\Omega = \Omega_f \cup \Omega_p \cup \mathbb{I}$. We choose the finite element spaces $Y_f^h \subset Y_f, Q_f^h \subset Q_f$; $Y_p^h \subset Y_p, Q_p^h \subset Q_p$; and $T_f^h \subset T_f, T_p^h \subset T_p$.

In the free flow region, we select finite element spaces (Y_f^h, Q_f^h) for velocity and pressure of the Navier–Stokes equation such that (Y_f^h, Q_f^h) satisfy the inf-sup condition, i.e., there exists a strictly positive constant $\chi_f > 0$ independent of mesh size h such that

$$\inf_{0\neq q^h \in Q_f^h} \sup_{0\neq \vec{v}_f^h \in Y_f^h} \frac{(q^h, \nabla\cdot\vec{v}_f^h)_{\Omega_f}}{||\nabla\vec{v}_f^h||_{L^2(\Omega_f)}||q^h||_{L^2(\Omega_f)}} \ge \chi_f.$$

Define the space of discretely divergence-free velocities:

$$\vec{V}_f^h = \{\vec{v}_f \in Y_f^h : (q, \nabla\cdot\vec{v}_f)_{\Omega_f} = 0 \ \ \forall\, q \in Q_f^h\}.$$

In the porous region, we select finite element spaces (Y_p^h, Q_p^h) that also satisfy the inf-sup conditions for velocity and pressure. That is, there exists a strictly positive constant χ_p, such that for all $\psi^h \in Q_p^h$ we have

$$\chi_p \|\psi^h\|_{L^2(\Omega_p)} \le \sup_{0\neq\vec{v}_p^h\in Y_p^h} \frac{(\psi^h, \nabla\cdot\vec{v}_p^h)_{\Omega_p}}{||\vec{v}_p^h||_{\mathrm{div}}},$$
$$\text{where } \|\vec{v}_p^h||_{\mathrm{div}} = \left(\|\vec{v}_p^h\|^2_{L^2(\Omega_p)} + \|\nabla\cdot\vec{v}_p^h\|^2_{L^2(\Omega_p)}\right)^{1/2}.$$

We assume that there is a constant C_{inv} which depends on the minimum angle in the finite element mesh used in the subdomain Ω_f, such that we have discrete local inverse inequality [60, 102, 86, 48, 18]

$$\|\nabla\theta_f^h\|_{L^2(\mathbb{I})} \le C_{inv}^{1/2} h^{-1/2} ||\nabla\theta_f^h||_{L^2(\Omega_f)} \qquad \forall\, \theta_f^h \in T_f^h. \tag{3.26}$$

Now we present the regular coupled finite element method based on the stabilized variational formulation (3.4)–(3.7). Set $\Delta t = \frac{T}{N}$ for a positive integer N and $t_n = n\Delta t$ $(n = 0, 1, 2, 3, \ldots, N)$. Then $\forall(\vec{v}_f^h, \vec{v}_p^h; q^h, \psi^h; \varphi^h, \omega^h) \in (Y_f^h, Y_p^h; Q_f^h, Q_p^h; T_f^h, T_p^h)$, find $(\vec{u}_f^{h,n+1}, \vec{u}_p^{h,n+1}; p_f^{h,n+1}, \phi_p^{h,n+1}; \theta_f^{h,n+1}, \theta_p^{h,n+1}) \in (Y_f^h, Y_p^h; Q_f^h, Q_p^h; T_f^h, T_p^h)$ such that

(3.27)
$$\left(\frac{\vec{u}_f^{h,n+1}-\vec{u}_f^{h,n}}{\Delta t},\vec{v}_f^h\right)_{\Omega_f}+C_aDa\left(\frac{\vec{u}_p^{h,n+1}-\vec{u}_p^{h,n}}{\Delta t},\vec{v}_p^h\right)_{\Omega_p}-(p_f^{h,n+1},\nabla\cdot\vec{v}_f^h)_{\Omega_f}$$
$$+Pr(\nabla\vec{u}_f^{h,n+1},\nabla\vec{v}_f^h)_{\Omega_f}+c^{\mathrm{tri}}(\vec{u}_f^{h,n+1},\vec{u}_f^{h,n+1},\vec{v}_f^h)_{\Omega_f}+Pr(\vec{u}_p^{h,n+1},\vec{v}_p^h)_{\Omega_p}$$
$$-Da(\phi_p^{h,n+1},\nabla\cdot\vec{v}_p^h)_{\Omega_p}=PrRa(\vec{\xi}\theta_f^{h,n+1},\vec{v}_f^h)_{\Omega_f}$$
$$+PrDaRa(\vec{\xi}\theta_p^{h,n+1},\vec{v}_p^h)_{\Omega_p}+(\vec{f}_f(t_{n+1}),\vec{v}_f^h)_{\Omega_f},$$

(3.28)
$$(q^h,\nabla\cdot\vec{u}_f^{h,n+1})_{\Omega_f}=0,$$

(3.29)
$$Da(\psi^h,\nabla\cdot\vec{u}_p^{h,n+1})_{\Omega_p}=0,$$

(3.30)
$$\left(\frac{\theta_f^{h,n+1}-\theta_f^{h,n}}{\Delta t},\varphi^h\right)_{\Omega_f}+\left(\frac{\theta_p^{h,n+1}-\theta_p^{h,n}}{\Delta t},\omega^h\right)_{\Omega_p}+k_f(\nabla\theta_f^{h,n+1},\nabla\varphi^h)_{\Omega_f}$$
$$+k_p(\nabla\theta_p^{h,n+1},\nabla\omega^h)_{\Omega_p}+t_f^{\mathrm{tri}}(\vec{u}_f^{h,n+1},\theta_f^{h,n+1},\varphi^h)_{\Omega_f}$$
$$+t_p^{\mathrm{tri}}(\vec{u}_p^{h,n+1},\theta_p^{h,n+1},\omega^h)_{\Omega_p}-k_f\int_{\mathbb{I}}\hat{n}_f\cdot\nabla\theta_f^{h,n+1}\cdot(\varphi^h-\omega^h)dl$$
$$+\frac{k_f\gamma}{h}\int_{\mathbb{I}}(\theta_f^{h,n+1}-\theta_p^{h,n+1})(\varphi^h-\omega^h)dl=(\Upsilon_f(t_{n+1}),\varphi^h)_{\Omega_f}+(\Upsilon_p(t_{n+1}),\omega^h)_{\Omega_p}.$$

4. The decoupled stabilized finite element method. Based on the above traditional coupled finite element method, in this section we propose and analyze the following decoupled stabilized finite element method, which is more efficient in practice. The key idea for the decoupled algorithm construction is to make the scheme as parallel as possible while good enough stability can be theoretically guaranteed: $\forall(\vec{v}_f^h,q^h,\varphi^h)\in(Y_f^h,Q_f^h,T_f^h)$ and $(\vec{v}_p^h,\psi^h,\omega^h)\in(Y_p^h,Q_p^h,T_p^h)$, find $(\vec{u}_f^{h,n+1},p_f^{h,n+1},\theta_f^{h,n+1})\in(Y_f^h,Q_f^h,T_f^h)$ and $(\vec{u}_p^{h,n+1},\phi_p^{h,n+1},\theta_p^{h,n+1})\in(Y_p^h,Q_p^h,T_p^h)$ such that

- *Step* 1:

$$\left(\frac{\vec{u}_f^{h,n+1}-\vec{u}_f^{h,n}}{\Delta t},\vec{v}_f^h\right)_{\Omega_f}-(p_f^{h,n+1},\nabla\cdot\vec{v}_f^h)_{\Omega_f}+Pr(\nabla\vec{u}_f^{h,n+1},\nabla\vec{v}_f^h)_{\Omega_f}$$
(4.1) $$+c^{\mathrm{tri}}(\vec{u}_f^{h,n},\vec{u}_f^{h,n+1},\vec{v}_f^h)_{\Omega_f}=PrRa(\vec{\xi}\theta_f^{h,n},\vec{v}_f^h)_{\Omega_f}+(\vec{f}_f(t_{n+1}),\vec{v}_f^h)_{\Omega_f},$$
(4.2) $$(q^h,\nabla\cdot\vec{u}_f^{h,n+1})_{\Omega_f}=0;$$

- *Step* 2:

(4.3)
$$\left(\frac{\theta_f^{h,n+1}-\theta_f^{h,n}}{\Delta t},\varphi^h\right)_{\Omega_f}+k_f(\nabla\theta_f^{h,n+1},\nabla\varphi^h)_{\Omega_f}+t_f^{\mathrm{tri}}(\vec{u}_f^{h,n},\theta_f^{h,n+1},\varphi^h)_{\Omega_f}$$
$$-k_f\int_{\mathbb{I}}\hat{n}_f\cdot\nabla\theta_f^{h,n}\varphi^h dl+\frac{k_f\gamma}{h}\int_{\mathbb{I}}(\theta_f^{h,n+1}-\theta_p^{h,n})\varphi^h dl=(\Upsilon_f(t_{n+1}),\varphi^h)_{\Omega_f};$$

- *Step* 3:

(4.4)

$$C_aDa\left(\frac{\vec{u}_p^{h,n+1}-\vec{u}_p^{h,n}}{\Delta t},\vec{v}_p^h\right)_{\Omega_p}+Pr(\vec{u}_p^{h,n+1},\vec{v}_p^h)_{\Omega_p}-Da(\phi_p^{h,n+1},\nabla\cdot\vec{v}_p^h)_{\Omega_p}$$
$$=PrDaRa(\vec{\xi}\theta_p^{h,n},\vec{v}_p^h)_{\Omega_p},$$

(4.5)
$$Da(\psi^h,\nabla\cdot\vec{u}_p^{h,n+1})_{\Omega_p}=0;$$

- *Step* 4:

(4.6)
$$\left(\frac{\theta_p^{h,n+1}-\theta_p^{h,n}}{\Delta t},\omega^h\right)_{\Omega_p}+k_p(\nabla\theta_p^{h,n+1},\nabla\omega^h)_{\Omega_p}+t_p^{\mathrm{tri}}(\vec{u}_p^{h,n},\theta_p^{h,n+1},\omega^h)_{\Omega_p}$$
$$+k_f\int_{\mathbb{I}}\hat{n}_f\cdot\nabla\theta_f^{h,n}\omega^h dl-\frac{k_f\gamma}{h}\int_{\mathbb{I}}(\theta_f^{h,n+1}-\theta_p^{h,n+1})\omega^h dl=(\Upsilon_p(t_{n+1}),\omega^h)_{\Omega_p}.$$

Now we analyze the stability of the above decoupled stabilized finite element method.

THEOREM 4.1. *Assume that* $\vec{f}_f\in L^2(0,T;H^{-1}(\Omega_f))$, $\Upsilon_f\in L^2(0,T;H^{-1}(\Omega_f))$, $\Upsilon_p\in L^2(0,T;H^{-1}(\Omega_p))$. *The stabilized decoupled scheme* (4.1)–(4.6) *is stable if the penalty parameter satisfies the condition* $\gamma>2C_{inv}$, *where* $C_{inv}>0$.

Proof. Choose $\vec{v}_f^h=2\Delta t\vec{u}_f^{h,n+1}$, $q^h=2\Delta t p_f^{h,n+1}$, $\varphi^h=2\Delta t\theta_f^{h,n+1}$, $\vec{v}_p^h=2\Delta t\vec{u}_p^{h,n+1}$, $\psi^h=2\Delta t\phi_p^{h,n+1}$, $\omega^h=2\Delta t\theta_p^{h,n+1}$ in (4.1), (4.2), (4.3), (4.4), (4.5), and (4.6), respectively. Adding these equations together and applying the condition $2(a-b,a)=(\|a\|^2-\|b\|^2+\|a-b\|^2)$, we obtain

(4.7)
$$\left[\|\vec{u}_f^{h,n+1}\|^2_{L^2(\Omega_f)}+\|\vec{u}_f^{h,n+1}-\vec{u}_f^{h,n}\|^2_{L^2(\Omega_f)}-\|\vec{u}_f^{h,n}\|^2_{L^2(\Omega_f)}\right]+\left[\|\theta_f^{h,n+1}\|^2_{L^2(\Omega_f)}\right.$$
$$\left.+\|\theta_f^{h,n+1}-\theta_f^{h,n}\|^2_{L^2(\Omega_f)}-\|\theta_f^{h,n}\|^2_{L^2(\Omega_f)}\right]+C_aDa\left[\|\vec{u}_p^{h,n+1}\|^2_{L^2(\Omega_p)}+\|\vec{u}_p^{h,n+1}\right.$$
$$\left.-\vec{u}_p^{h,n}\|^2_{L^2(\Omega_p)}-\|\vec{u}_p^{h,n}\|^2_{L^2(\Omega_p)}\right]+\left[\|\theta_p^{h,n+1}\|^2_{L^2(\Omega_p)}\right.$$
$$\left.+\|\theta_p^{h,n+1}-\theta_p^{h,n}\|^2_{L^2(\Omega_p)}-\|\theta_p^{h,n}\|^2_{L^2(\Omega_p)}\right]+2Pr\Delta t\|\nabla\vec{u}_f^{h,n+1}\|^2_{L^2(\Omega_f)}$$
$$+2\Delta tPr\|\vec{u}_p^{h,n+1}\|^2_{L^2(\Omega_p)}+2\Delta tk_f\|\nabla\theta_f^{h,n+1}\|^2_{L^2(\Omega_f)}+2\Delta tk_p\|\nabla\theta_p^{h,n+1}\|^2_{L^2(\Omega_p)}$$
$$=2PrRa\Delta t(\vec{\xi}\theta_f^{h,n},\vec{u}_f^{h,n+1})_{\Omega_f}+2\Delta t(\vec{f}_f(t_{n+1}),\vec{u}_f^{h,n+1})_{\Omega_f}$$
$$+2\Delta t(\Upsilon_f(t_{n+1}),\theta_f^{h,n+1})_{\Omega_f}+2PrDaRa\Delta t(\vec{\xi}\theta_p^{h,n},\vec{u}_p^{h,n+1})_{\Omega_p}$$
$$+2\Delta t(\Upsilon_p(t_{n+1}),\theta_p^{h,n+1})_{\Omega_p}+2k_f\Delta t\int_{\mathbb{I}}\hat{n}_f\cdot\nabla\theta_f^{h,n}(\theta_f^{h,n+1}-\theta_p^{h,n+1})dl$$
$$-\frac{2k_f\gamma\Delta t}{h}\int_{\mathbb{I}}(\theta_f^{h,n+1}-\theta_p^{h,n})\theta_f^{h,n+1}dl+\frac{2k_f\gamma\Delta t}{h}\int_{\mathbb{I}}(\theta_f^{h,n+1}-\theta_p^{h,n+1})\theta_p^{h,n+1}dl.$$

Using the Cauchy–Schwarz inequality and Young's inequality, the terms on the right-

hand side of (4.7) can be estimated as follows:

$$2PrRa\Delta t(\vec{\xi}\theta_f^{h,n}, \vec{u}_f^{h,n+1})_{\Omega_f} \le PrRa^2\Delta t\|\theta_f^{h,n}\|^2_{L^2(\Omega_f)} + Pr\Delta t\|\vec{u}_f^{h,n+1}\|^2_{L^2(\Omega_f)}, \tag{4.8}$$

where $\vec{\xi} = [0,1]^T$,

$$2\Delta t(\vec{f}_f(t_{n+1}), \vec{u}_f^{h,n+1})_{\Omega_f} \le \frac{\Delta t}{Pr}\|\vec{f}_f(t_{n+1})\|^2_{H^{-1}(\Omega_f)} + Pr\Delta t\|\nabla\vec{u}_f^{h,n+1}\|^2_{L^2(\Omega_f)}, \tag{4.9}$$

$$2\Delta t(\Upsilon_f(t_{n+1}), \theta_f^{h,n+1})_{\Omega_f} \le \frac{\Delta t}{k_f}\|\Upsilon_f(t_{n+1})\|^2_{H^{-1}(\Omega_f)} + k_f\Delta t\|\nabla\theta_f^{h,n+1}\|^2_{L^2(\Omega_f)}, \tag{4.10}$$

$$2PrDaRa\Delta t(\vec{\xi}\theta_p^{h,n}, \vec{u}_p^{h,n+1})_{\Omega_p} \le PrDa^2Ra^2\Delta t\|\theta_p^{h,n}\|^2_{L^2(\Omega_p)} + Pr\Delta t\|\vec{u}_p^{h,n+1}\|^2_{L^2(\Omega_p)}, \tag{4.11}$$

$$2\Delta t(\Upsilon_p(t_{n+1}), \theta_p^{h,n+1})_{\Omega_p} \le \frac{\Delta t}{k_p}\|\Upsilon_p(t_{n+1})\|^2_{H^{-1}(\Omega_p)} + k_p\Delta t\|\nabla\theta_p^{h,n+1}\|^2_{L^2(\Omega_p)}. \tag{4.12}$$

Applying discrete local inverse inequality, we obtain

$$\begin{aligned} 2k_f\Delta t\int_{\mathbb{I}}\hat{n}_f\cdot\nabla\theta_f^{h,n}(\theta_f^{h,n+1}-\theta_p^{h,n+1})dl &\\ &\le 2k_f\Delta t\|\hat{n}_f\cdot\nabla\theta_f^{h,n}\|_{L^2(\mathbb{I})}\|\theta_f^{h,n+1}-\theta_p^{h,n+1}\|_{L^2(\mathbb{I})}\\ &\le 2k_fC_{inv}^{1/2}h^{-1/2}\Delta t\|\nabla\theta_f^{h,n}\|_{L^2(\Omega_f)}\|\theta_f^{h,n+1}-\theta_p^{h,n+1}\|_{L^2(\mathbb{I})}\\ &\le \frac{2k_fC_{inv}\Delta t}{\gamma}\|\nabla\theta_f^{h,n}\|^2_{L^2(\Omega_f)} + \frac{k_f\gamma\Delta t}{2h}\|\theta_f^{h,n+1}-\theta_p^{h,n+1}\|^2_{L^2(\mathbb{I})}. \end{aligned} \tag{4.13}$$

Applying the equality condition $(a-b,a) = \frac{1}{2}(\|a\|^2 - \|b\|^2 + \|a-b\|^2)$, the Cauchy–Schwarz inequality, and Young's inequality, we can achieve

$$\begin{aligned} -\frac{2k_f\gamma\Delta t}{h}\int_{\mathbb{I}}(\theta_f^{h,n+1}-\theta_p^{h,n})\theta_f^{h,n+1}dl + \frac{2k_f\gamma\Delta t}{h}\int_{\mathbb{I}}(\theta_f^{h,n+1}-\theta_p^{h,n+1})\theta_p^{h,n+1}dl &\\ = -\frac{2k_f\gamma\Delta t}{h}\|\theta_f^{h,n+1}-\theta_p^{h,n+1}\|^2_{L^2(\mathbb{I})} - \frac{2k_f\gamma\Delta t}{h}\Big[\int_{\mathbb{I}}(\theta_p^{h,n+1}-\theta_p^{h,n})\theta_p^{h,n+1}dl &\\ -\int_{\mathbb{I}}(\theta_p^{h,n+1}-\theta_p^{h,n})(\theta_p^{h,n+1}-\theta_f^{h,n+1})dl\Big] &\\ \le -\frac{2k_f\gamma\Delta t}{h}\|\theta_f^{h,n+1}-\theta_p^{h,n+1}\|^2_{L^2(\mathbb{I})} - \frac{k_f\gamma\Delta t}{h}\Big[\|\theta_p^{h,n+1}\|^2_{L^2(\mathbb{I})} &\\ -\|\theta_p^{h,n}\|^2_{L^2(\mathbb{I})} - \|\theta_f^{h,n+1}-\theta_p^{h,n+1}\|^2_{L^2(\mathbb{I})}\Big]. \end{aligned} \tag{4.14}$$

Inserting (4.8)–(4.14) into (4.7) and taking the sum from $n=0$ to $l-1$, we obtain

$$\|\vec{u}_f^{h,l}\|^2_{L^2(\Omega_f)} + \sum_{n=0}^{l-1}\|\vec{u}_f^{h,n+1}-\vec{u}_f^{h,n}\|^2_{L^2(\Omega_f)} + \|\theta_f^{h,l}\|^2_{L^2(\Omega_f)} + \sum_{n=0}^{l-1}\|\theta_f^{h,n+1}-\theta_f^{h,n}\|^2_{L^2(\Omega_f)} \tag{4.15}$$

$$
\begin{aligned}
&+C_aDa\|\vec{u}_p^{h,l}\|^2_{L^2(\Omega_p)}+C_aDa\sum_{n=0}^{l-1}\|\vec{u}_p^{h,n+1}-\vec{u}_p^{h,n}\|^2_{L^2(\Omega_p)}+\|\theta_p^{h,l}\|^2_{L^2(\Omega_p)}\\
&+\sum_{n=0}^{l-1}\|\theta_p^{h,n+1}-\theta_p^{h,n}\|^2_{L^2(\Omega_p)}+2Pr\Delta t\sum_{n=0}^{l-1}\|\nabla\vec{u}_f^{h,n+1}\|^2_{L^2(\Omega_f)}\\
&+2Pr\Delta t\sum_{n=0}^{l-1}\|\vec{u}_p^{h,n+1}\|^2_{L^2(\Omega_p)}+2k_f\Delta t\sum_{n=0}^{l-1}\|\nabla\theta_f^{h,n+1}\|^2_{L^2(\Omega_f)}+2k_p\Delta t\sum_{n=0}^{l-1}\|\nabla\theta_p^{h,n+1}\|^2_{L^2(\Omega_p)}\\
&\quad\le PrRa^2\Delta t\sum_{n=0}^{l-1}\|\theta_f^{h,n}\|^2_{L^2(\Omega_f)}+Pr\Delta t\sum_{n=0}^{l-1}\|\vec{u}_f^{h,n+1}\|^2_{L^2(\Omega_f)}\\
&+\frac{\Delta t}{Pr}\sum_{n=0}^{l-1}\|\vec{f}_f(t_{n+1})\|^2_{H^{-1}(\Omega_f)}\\
&+Pr\Delta t\sum_{n=0}^{l-1}\|\nabla\vec{u}_f^{h,n+1}\|^2_{L^2(\Omega_f)}+\frac{\Delta t}{k_f}\sum_{n=0}^{l-1}\|\Upsilon_f(t_{n+1})\|^2_{H^{-1}(\Omega_f)}\\
&+k_f\Delta t\sum_{n=0}^{l-1}\|\nabla\theta_f^{h,n+1}\|^2_{L^2(\Omega_f)}+\frac{\Delta t}{k_p}\sum_{n=0}^{l-1}\|\Upsilon_p(t_{n+1})\|^2_{H^{-1}(\Omega_p)}\\
&+k_p\Delta t\sum_{n=0}^{l-1}\|\nabla\theta_p^{h,n+1}\|^2_{L^2(\Omega_p)}+PrDa^2Ra^2\Delta t\sum_{n=0}^{l-1}\|\theta_p^{h,n}\|^2_{L^2(\Omega_p)}\\
&+Pr\Delta t\sum_{n=0}^{l-1}\|\vec{u}_p^{h,n+1}\|^2_{L^2(\Omega_p)}+\frac{2k_fC_{inv}\Delta t}{\gamma}\sum_{n=0}^{l-1}\|\nabla\theta_f^{h,n}\|^2_{L^2(\Omega_f)}\\
&+\frac{k_f\gamma\Delta t}{2h}\sum_{n=0}^{l-1}\|\theta_f^{h,n+1}-\theta_p^{h,n+1}\|^2_{L^2(\mathbb{I})}\\
&-\frac{k_f\gamma\Delta t}{h}\sum_{n=0}^{l-1}\|\theta_f^{h,n+1}-\theta_p^{h,n+1}\|^2_{L^2(\mathbb{I})}-\frac{k_f\gamma\Delta t}{h}\|\theta_p^{h,l}\|^2_{L^2(\mathbb{I})}+\frac{k_f\gamma\Delta t}{h}\|\theta_p^{h,0}\|^2_{L^2(\mathbb{I})}\\
&+\|\vec{u}_f^{h,0}\|^2_{L^2(\Omega_f)}+C_aDa\|\vec{u}_p^{h,0}\|^2_{L^2(\Omega_p)}+\|\theta_f^{h,0}\|^2_{L^2(\Omega_f)}+\|\theta_p^{h,0}\|^2_{L^2(\Omega_p)}.
\end{aligned}
$$

Rearranging (4.15) and using Gronwall's lemma, we have the following stability result:

(4.16)

$$
\begin{aligned}
&\|\vec{u}_f^{h,l}\|^2_{L^2(\Omega_f)}+\sum_{n=0}^{l-1}\|\vec{u}_f^{h,n+1}-\vec{u}_f^{h,n}\|^2_{L^2(\Omega_f)}+\|\theta_f^{h,l}\|^2_{L^2(\Omega_f)}+\sum_{n=0}^{l-1}\|\theta_f^{h,n+1}-\theta_f^{h,n}\|^2_{L^2(\Omega_f)}\\
&+C_aDa\|\vec{u}_p^{h,l}\|^2_{L^2(\Omega_p)}+C_aDa\sum_{n=0}^{l-1}\|\vec{u}_p^{h,n+1}-\vec{u}_p^{h,n}\|^2_{L^2(\Omega_p)}+\|\theta_p^{h,l}\|^2_{L^2(\Omega_p)}\\
&+\sum_{n=0}^{l-1}\|\theta_p^{h,n+1}-\theta_p^{h,n}\|^2_{L^2(\Omega_p)}+Pr\Delta t\sum_{n=0}^{l-1}\|\nabla\vec{u}_f^{h,n+1}\|^2_{L^2(\Omega_f)}+Pr\Delta t\sum_{n=0}^{l-1}\|\vec{u}_p^{h,n+1}\|^2_{L^2(\Omega_p)}\\
&+k_f\left(1-\frac{2C_{inv}}{\gamma}\right)\Delta t\sum_{n=0}^{l-1}\|\nabla\theta_f^{h,n+1}\|^2_{L^2(\Omega_f)}+k_p\Delta t\sum_{n=0}^{l-1}\|\nabla\theta_p^{h,n+1}\|^2_{L^2(\Omega_p)}
\end{aligned}
$$

$$+\frac{k_f\gamma\Delta t}{2h}\sum_{n=0}^{l-1}\|\theta_f^{h,n+1}-\theta_p^{h,n+1}\|^2_{L^2(\mathbb{I})}+\frac{k_f\gamma\Delta t}{h}\|\theta_p^{h,l}\|^2_{L^2(\mathbb{I})}$$
$$\le C\bigg(\frac{\Delta t}{Pr}\sum_{n=0}^{l-1}\|\vec{f}_f(t_{n+1})\|^2_{H^{-1}(\Omega_f)}+\frac{\Delta t}{k_f}\sum_{n=0}^{l-1}\|\Upsilon_f(t_{n+1})\|^2_{H^{-1}(\Omega_f)}$$
$$+\frac{\Delta t}{k_p}\sum_{n=0}^{l-1}\|\Upsilon_p(t_{n+1})\|^2_{H^{-1}(\Omega_p)}+\|\vec{u}_f^{h,0}\|^2_{L^2(\Omega_f)}+C_aDa\|\vec{u}_p^{h,0}\|^2_{L^2(\Omega_p)}$$
$$+\|\theta_f^{h,0}\|^2_{L^2(\Omega_f)}+\|\theta_p^{h,0}\|^2_{L^2(\Omega_p)}+\frac{2C_{inv}k_f\Delta t}{\gamma}\|\nabla\theta_f^{h,0}\|^2_{L^2(\Omega_f)}+\frac{k_f\gamma\Delta t}{h}\|\theta_p^{h,0}\|^2_{L^2(\mathbb{I})}\bigg).$$

The penalty parameter satisfies the condition $\gamma > 2C_{inv}$, where $C_{inv} > 0$, which completes the proof of the stability of the decoupled scheme. ∎

Remark 4.1. The stability of the coupled scheme can be similarly derived for the following conclusion.

THEOREM 4.2. *Assume that* $\vec{f}_f \in L^2(0,T;H^{-1}(\Omega_f))$, $\Upsilon_f \in L^2(0,T;H^{-1}(\Omega_f))$, $\Upsilon_p \in L^2(0,T;H^{-1}(\Omega_p))$. *The stabilized coupled scheme* (3.27)–(3.30) *is stable if the penalty parameter satisfies the condition* $\gamma > 2C_{inv}$, *where* $C_{inv} > 0$.

5. Numerical experiments. In this section, we present four numerical experiments to validate the proposed model and numerical methods. The first example with an analytic solution is provided to show the optimal convergence of the finite element solutions and the impact of the penalty parameter on the convergence. The second numerical test is conducted to investigate a benchmark problem for thermal convection in a squared cavity. The third example is to illustrate the applicability of the proposed model and numerical method to the closed-loop geothermal system by using a simplified set-up. In the fourth example, we demonstrate the effect of the curve interface on the temperature distribution for a closed-loop geothermal system.

The well-known MINI elements ($P1b-P1$) are used for the Navier–Stokes equation in the conduit domain Ω_f [77, 5]. Piecewise constant elements $P0$ are used for Darcy pressure ϕ_p, and Brezzi–Douglas–Marini (BDM1) finite elements are used for Darcy velocity $\vec{u}_p$ [15]. In both subdomains for temperature θ_f and θ_p, we use linear Lagrangian elements $P1$.

5.1. Convergence and stability tests. Assume the computational domain Ω consists of two subdomains. One is the free fluid flow region $\Omega_f = [0,1]\times[1,2]$, and the other one is the porous media region $\Omega_p = [0,1]\times[0,1]$. The interface between the free flow region and porous media is taken as $\mathbb{I} = (0,1)\times\{1\}$. Uniform triangular meshes are created by first partitioning the rectangular domain Ω_f, and Ω_p into identical square elements with the mesh size h, and then dividing each square into two triangles.

The selected exact solution for the model is given by

$$\text{(5.1)}\qquad \begin{cases} \vec{u}_f &:= \begin{pmatrix} 10x^2(x-1)^2y(y-1)(2y-1)cos(t) \\ -10x(x-1)(2x-1)y^2(y-1)^2cos(t) \end{pmatrix}, \\ p_f &:= 10(2x-1)(2y-1)cos(t), \\ \vec{u}_p &:= \begin{pmatrix} [2\pi sin^2(\pi x)sin(\pi y)cos(\pi y)]cos(t) \\ [-2\pi sin(\pi x)sin^2(\pi y)cos(\pi x)]cos(t) \end{pmatrix}, \\ \phi_p &:= cos(\pi x)cos(\pi y)cos(t), \\ \theta_f &:= ax(1-x)(1-y)e^{-t}, \\ \theta_p &:= ax(1-x)(y-y^2)e^{-t}. \end{cases}$$

The initial condition, boundary condition, and forcing term of the model problem (2.1)–(2.16) are chosen such that above functions are the exact solutions of the model problem. Choose the parameter values $a = 1.0$, $Pr = 1.0$, $Ra = 1.0$, $k_f = k_p = 1.0$, $C_a = 1.0$, $Da = 1.0$, $\gamma = 10^5$, $T = 0.5$, and $\Delta t = 0.001$. In the tables below, we denote the errors by using $e^{h,n}_{\Phi_\Lambda} = \Phi^{h,n}_\Lambda - \Phi_\Lambda(t^n)$, where $\Phi = \vec{u}$ or θ and $\Lambda = f$ or p.

TABLE 5.1

The errors in the L^2- and the H^1-norm for the decoupled stabilized scheme with different h and fixed $\Delta t = 0.001$ at the final time $T = 0.5$.

h	$\|\|e^{h,n}_{\vec{u}_f}\|\|_0$	Order	$\|\|e^{h,n}_{\theta_f}\|\|_0$	Order	$\|\|e^{h,n}_{\theta_p}\|\|_0$	Order	$\|\|e^{h,n}_{\vec{u}_p}\|\|_0$	Order
1/4	0.40846000		0.00468918		0.00341420		0.24790300	
1/8	0.10494300	1.9605	0.00116964	2.0032	0.00090792	1.9109	0.06573370	1.9150
1/16	0.02626210	1.9985	0.00029335	1.9953	0.00023107	1.9742	0.01671560	1.9754
1/32	0.00654013	2.0055	7.46087e-05	1.9752	5.86945e-05	1.9770	0.00423175	1.9818
1/64	0.00163015	2.0043	1.99111e-05	1.9057	1.54964e-05	1.9212	0.00118770	1.8330
h	$\|\|e^{h,n}_{\vec{u}_f}\|\|_1$	Order	$\|\|e^{h,n}_{\theta_f}\|\|_1$	Order	$\|\|e^{h,n}_{\theta_p}\|\|_1$	Order		
1/4	6.004770		0.0707448		0.03565450			
1/8	2.754750	1.1241	0.0356499	0.9887	0.01829400	0.9627		
1/16	1.275050	1.1113	0.0178589	0.9972	0.00920755	0.9904		
1/32	0.614009	1.0542	0.0089336	0.9993	0.00461145	0.9975		
1/64	0.302294	1.0223	0.0044673	0.9998	0.00230670	0.9993		

TABLE 5.2

The errors in the L^2-norm by using $\Delta t = h^2$ and in the H^1-norm by setting $\Delta t = h$ for the decoupled stabilized scheme at the final time $T = 0.5$.

h	Δt	$\|\|e^{h,n}_{\vec{u}_f}\|\|_0$	Order	$\|\|e^{h,n}_{\theta_f}\|\|_0$	Order	$\|\|e^{h,n}_{\theta_p}\|\|_0$	Order	$\|\|e^{h,n}_{\vec{u}_p}\|\|_0$	Order
1/4	1/16	0.40845800		0.0046804		0.00341434		0.2483770	
1/8	1/64	0.10494300	1.9605	0.0011609	2.0113	0.00090560	1.9146	0.0658987	1.9142
1/16	1/256	0.02626190	1.9985	0.0002912	1.9951	0.00023077	1.9723	0.0167671	1.9746
1/32	1/1024	0.00654014	2.0055	7.46291e-5	1.9642	5.86923e-05	1.9752	0.0042310	1.9865
1/64	1/4096	0.00163029	2.0041	2.08525e-5	1.8395	1.51408e-05	1.9547	0.0011338	1.8997
h	Δt	$\|\|e^{h,n}_{\vec{u}_f}\|\|_1$	Order	$\|\|e^{h,n}_{\theta_f}\|\|_1$	Order	$\|\|e^{h,n}_{\theta_p}\|\|_1$	Order		
1/4	1/4	6.004900		0.07110420		0.03578750			
1/8	1/8	2.754800	1.1241	0.03568050	0.9947	0.01831080	0.9667		
1/16	1/16	1.275060	1.1113	0.01785970	0.9984	0.00920847	0.9916		
1/32	1/32	0.614016	1.0542	0.00893396	0.9993	0.00461148	0.9977		
1/64	1/64	0.302297	1.0223	0.00446765	0.9997	0.00230671	0.9993		

Fixing the time step size $\Delta t = 0.001$, the errors with the varying spatial mesh size h for the decoupled stabilized finite element method are listed in Table 5.1. The data in this table illustrates that the decoupled method achieves optimal convergence rates in both the L^2-norm and the H^1-norm. It is well-known that the expected accuracy order is $O(h^2 + \Delta t)$ for the L^2-norm and $O(h + \Delta t)$ for the H^1-norm. In order to illustrate the second order accuracy in space, we set $\Delta t = h^2$ for the L^2-norm in Table 5.2. On the other hand, $\Delta t = h$ is used to illustrate the first order accuracy for the H^1-norm. From Table 5.2, we can observe that decoupled algorithm achieves optimal convergence order $O(h^2)$ in the L^2-norm and $O(h)$ in the H^1-norm.

TABLE 5.3
The effect of the penalty parameter on the convergence of the decoupled stabilized scheme.

h	$\gamma = 100000$	$\gamma = 1000$	$\gamma = 1$	$\gamma = 0.001$	$\gamma = 0$
			$\|\|e^{h,n}_{\vec{u}_f}\|\|_0$		
1/8	0.10494300	0.10494300	0.10494300	0.10494300	0.10494300
1/16	0.02626210	0.02626210	0.02626210	0.02626150	0.02626140
1/32	0.00654013	0.00654014	0.00654013	0.00653956	0.00653949
1/64	0.00163015	0.00163015	0.00163016	0.00162972	0.00162953
			$\|\|e^{h,n}_{\theta_f}\|\|_0$		
1/8	0.00116964	0.00122413	0.00111323	0.00549877	0.00561255
1/16	0.00029335	0.00033928	0.00028941	0.00423029	0.00459165
1/32	7.46087e-05	0.00010939	8.82900e-05	0.00304907	0.00411020
1/64	1.99111e-05	4.35675e-05	4.96786e-05	0.00162527	0.00382343
			$\|\|e^{h,n}_{\vec{u}_p}\|\|_0$		
1/8	0.06573370	0.06573370	0.06573330	0.06573710	0.06573730
1/16	0.01671560	0.01671540	0.01671450	0.01671480	0.01671540
1/32	0.00423175	0.00423137	0.00422762	0.00422308	0.00422843
1/64	0.00118770	0.00118701	0.00117328	0.00114516	0.00117924
			$\|\|e^{h,n}_{\theta_p}\|\|_0$		
1/8	0.00090792	0.00081944	0.00093210	0.00510302	0.00521338
1/16	0.00023107	0.00018811	0.00023835	0.00421036	0.00456259
1/32	5.86945e-05	5.52669e-05	4.86616e-05	0.00312289	0.00416500
1/64	1.54964e-05	2.68732e-05	2.69064e-05	0.00170941	0.00389860

The stability analysis results of the stabilized coupled and decoupled schemes are provided in Theorems 4.1 and 4.2, which require the condition $\gamma > 2C_{inv}$, where C_{inv} is strictly positive. In the following, we investigate the impact of the penalty parameter γ on the convergence. In Table 5.3, we list the errors $||e^{h,n}_{\vec{u}_f}||_0, ||e^{h,n}_{\theta_f}||_0, ||e^{h,n}_{\vec{u}_p}||_0$, and $||e^{h,n}_{\theta_p}||_0$ with respect to different values of the penalty parameter. The table verifies that a large enough penalty parameter is necessary to guarantee the stability and hence the convergence. Furthermore, one can observe that a larger penalty parameter provides better convergence performance for θ_f and θ_p, which is expected based on the explanations in Remark 3.1.

5.2. Convection in a squared cavity. We construct this model problem inspired by the natural convection in a cavity called Rayleigh–Bénard convection which is often considered as a benchmark problem [108, 39, 105, 109]. This experiment is extended by adding another subdomain for the porous media region and then simulating for the proposed coupled multiphysics model.

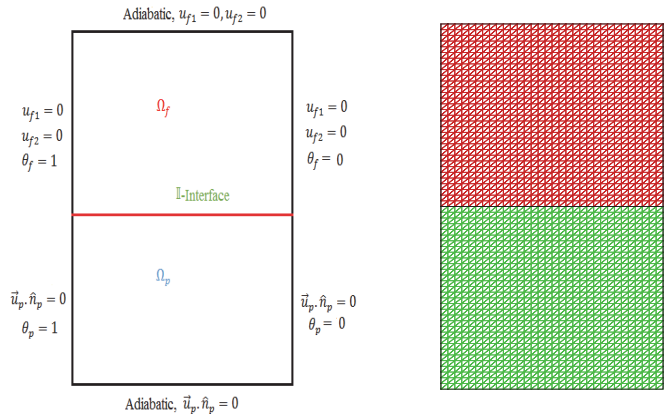

FIG. 5.1. *A sketch of the computational domain with boundary conditions (left) and the illustration of mesh (right).*

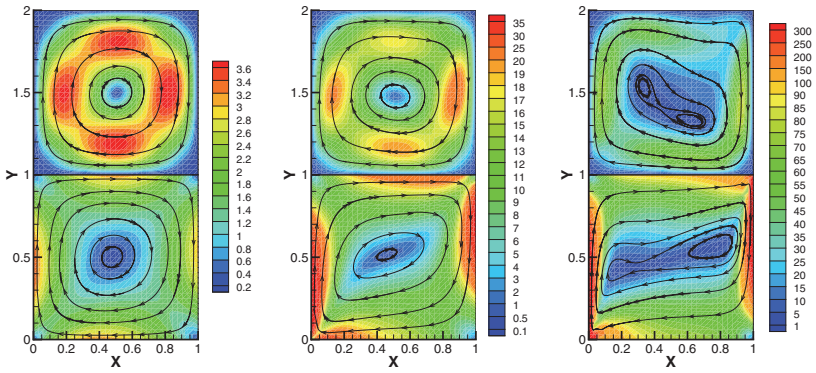

FIG. 5.2. *The streamlines and magnitudes of velocity for different values of Rayleigh number. Left:* $Ra = 10^3$. *Middle:* $Ra = 10^4$. *Right:* $Ra = 10^5$.

Assume the computational domain is $\Omega_f = [0,1] \times [1,2]$ and $\Omega_p = [0,1] \times [0,1]$ with a common interface $\mathbb{I} = (0,1) \times \{1\}$. The boundary conditions are illustrated in Figure 5.1. The no-slip boundary condition for the conduit region and the no-flow boundary condition on the porous media region are imposed on all of the boundaries:

$$\vec{u}_f = 0 \quad \text{on } \partial\Omega_f \setminus \mathbb{I} \quad \text{and} \quad \vec{u}_p \cdot \hat{n}_p = 0 \quad \text{on } \partial\Omega_p \setminus \mathbb{I}. \tag{5.2}$$

The left boundary is considered as a heated wall with $\theta_f = \theta_p = 1$, and the right

boundary is a cold wall with $\theta_f = \theta_p = 0$. On the top and bottom boundaries, we consider an insulated situation by applying $\hat{n}_f \cdot k_f \nabla\theta_f = 0$ and $\hat{n}_p \cdot k_p \nabla\theta_p = 0$, respectively. On the interface between the two regions, the interface conditions (2.20)–(2.23), which are proposed for the model, are utilized.

The parameters are chosen as $k_f = k_p = 1.0$, $C_a = 1.0$, $Pr = 0.71$, $10^3 \leq Ra \leq 10^5$, and $Da = 1.0 \times 10^{-2}$ [108, 39, 105]. We also choose $\gamma = 1.0$, $T = 3.0$, and $\Delta t = 0.01$. The initial values for velocity and temperature in both subdomains are chosen to be 0 and 1, respectively. The external body forces $\vec{f}_f$, Υ_f, and Υ_p are simply taken as zero. The mesh is constructed in the same way as in example (5.1) with $h = 1/32$.

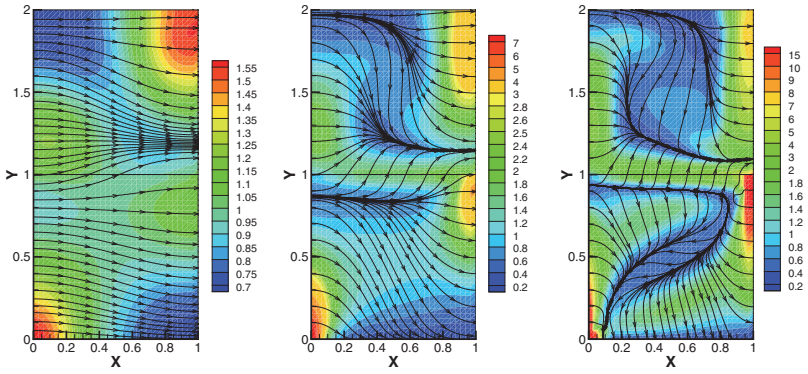

FIG. 5.3. *The streamlines and magnitudes of heat flux for different values of Rayleigh number. Left:* $Ra = 10^3$. *Middle:* $Ra = 10^4$. *Right:* $Ra = 10^5$.

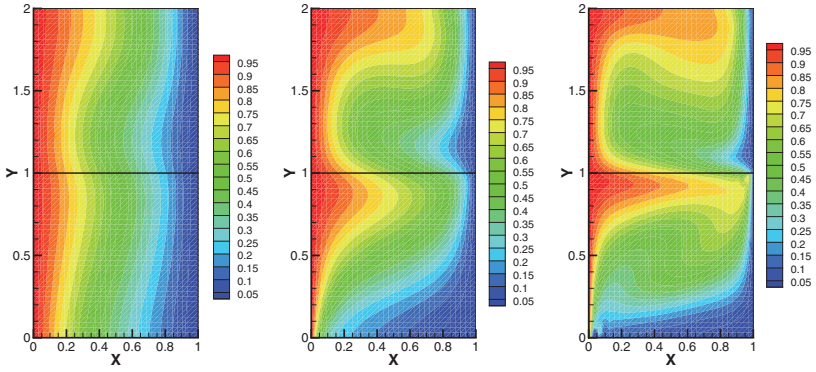

FIG. 5.4. *The temperature distribution for different values of Rayleigh number. Left:* $Ra = 10^3$. *Middle:* $Ra = 10^4$. *Right:* $Ra = 10^5$.

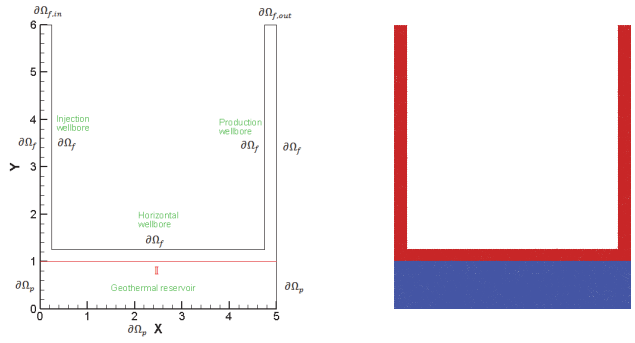

FIG. 5.5. *The U-shape domain consists of closed-loop heat exchanging pipelines Ω_f and geothermal reservoir Ω_p, separated by a common interface $\mathbb{I}$ (left) and illustration of mesh (right).*

In Figures 5.2, 5.3, and 5.4, we demonstrate the velocity field, heat flux, and temperature distribution with respect to different Rayleigh numbers. From Figure 5.2, it is clear that the streamlines are more circular when the Rayleigh numbers are 10^3 and 10^4. When the Rayleigh number is increased to 10^5, the circular vortex in Ω_f tends to be deformed into an ellipse and then break up, which coincides with the studies in [108, 39, 105, 109], while the whole field is also affected by the heat transfer through the interface from the porous media part. From the streamlines of velocity, we can also see that the no-fluid-communication interface condition is enforced. Based on Figures 5.3 and 5.4, the thermal convection increases rapidly when the Rayleigh number is increased. These physically valid simulation results validate the proposed model and numerical method.

5.3. Simulation for a closed-loop geothermal system. In this example, we simulate the flow behavior, heat flux, and thermal convection in a simplified closed-loop geothermal system. As shown in Figure 5.5, the conduit domain consists of a U-shape closed-loop heat exchange pipeline where the cold fluid can be injected through the vertical injection well on the left and the heated outflow can be pumped out from the vertical production well on the right [92, 95, 35]. In the porous medium, we consider a geothermal reservoir as the source of heat energy and thermal convection.

Based on the simulation of a fundamental case, for which we will show all of the velocity field, heat flux, and temperature distribution, we will investigate the effect of several different sets of the parameters, including the length of simulation time, Darcy number, thermal conductivity, the length of the horizontal well, and injection temperature. The results will be illustrated only by the temperature distribution due to its importance and the page limitation.

The inflow boundary condition is imposed on the top boundary $\partial\Omega_{f\,\mathrm{in}} = \{(x, y) : y = 6, 0 \leqslant x \leqslant 0.25\}$ with $U_x = 0$ and $U_y = -2048.0x(0.25-x)$ of the vertical injection well on the left. The boundary condition for temperature is assumed as $\theta_f = 20$ for the same boundary. The initial condition for the velocity and temperature of the closed-loop pipe is assumed as $\vec{u}_f(0, x) = (0, 0)$ and $\theta_f(0, x) = 20$, respectively. On the top boundary $\partial\Omega_{f\,\mathrm{out}} = \{(x, y) : y = 6, 4.75 \leqslant x \leqslant 5\}$ of the vertical production well on the right, the free outflow boundary conditions are imposed:

$$(-p_f\mathbf{I} + Pr\nabla\vec{u}_f) \cdot \hat{n}_f = 0, \qquad \hat{n}_f \cdot k_f \nabla\theta_f = 0 \quad \text{on} \quad \partial\Omega_{f\,\mathrm{out}}. \tag{5.3}$$

On the other boundaries of the closed-loop pipe $\{(x, y) : x = 0, 1 \leqslant y \leqslant 6\} \subset \partial\Omega_f$,

$\{(x,y) : x = 0.25, 1.25 \leqslant y \leqslant 6\} \subset \partial\Omega_f$, $\{(x,y) : y = 1.25, 0.25 \leqslant x \leqslant 4.75\} \subset \partial\Omega_f$, $\{(x,y) : x = 4.75, 1.25 \leqslant y \leqslant 6\} \subset \partial\Omega_f$, and $\{(x,y) : x = 5, 1 \leqslant y \leqslant 6\} \subset \partial\Omega_f$, we impose the no-slip boundary condition for velocity and the insulated boundary condition for temperature:

$$\vec{u}_f = 0, \qquad \hat{n}_f \cdot k_f \nabla\theta_f = 0 \quad \text{on } \partial\Omega_f \setminus \mathbb{I}. \tag{5.4}$$

On the interface $\mathbb{I} = \{(x,y) : y = 1, 0 \leqslant x \leqslant 5\}$, the interface conditions (2.20)–(2.23), which are proposed for the model, are utilized.

The geothermal reservoir domain is $\Omega_p = [0,5] \times [0,1]$. We impose the no-flow boundary condition $\vec{u}_p \cdot \hat{n}_p = 0$ on $\partial\Omega_p \setminus \mathbb{I}$. The homogeneous Neumann boundary condition is considered for the temperature on the left and right walls of Ω_p. In the bottom of the reservoir, we consider a hot wall by imposing $\theta_p = 100$. The initial condition for the velocity and temperature of the reservoir region is assumed as $\vec{u}_p(0,x) = (0,0)$, and $\theta_p(0,x) = 100$, respectively.

For the fundamental simulation, the parameters are chosen as $k_f = 0.6$, $k_p = 1.0$, $Pr = 3.0$, $Ra = 10^4$, $C_a = 1.0$, $Da = 1.0 \times 10^{-6}$, and $\gamma = 1.0$. The external body forces $\vec{f}_f$, Υ_f, and Υ_p are simply taken as zero. We construct the mesh with the mesh size $h_{max} = 0.05$, and use the time step size $\Delta t = 0.01$ with final time $T = 3.0$. The velocity field, heat flux, and temperature distribution of this case are shown in Figure 5.6. As expected, the heat fluxes move from the geothermal reservoir to the pipelines across the interface, while the velocity streamlines clearly indicate that the no-fluid-communication interface conditions are enforced. In the left part of the horizontal well, which is close to the injection well, the continuously injected cold water starts to get in contact with the geothermal reservoir of high temperature, which leads to a faster heat flux transmission. Moreover, the faster and slower flows can be observed in the pipe region and geothermal reservoir, respectively, which is physically valid. The effect of the no-slip boundary condition can also be observed in the pipe region where the speed is higher in the middle of the pipe. In the porous media domain, we can see a fluid circulation formed by the relatively hotter fluid in the lower part of the reservoir and the relatively colder fluid near the horizontal well, which is due to the natural convection. From the reasonable temperature distribution, one can see that the cold water is injected down from the left vertical well to the horizontal well, heated by the geothermal reservoir, and then pumped out from the right vertical well with much higher production temperature.

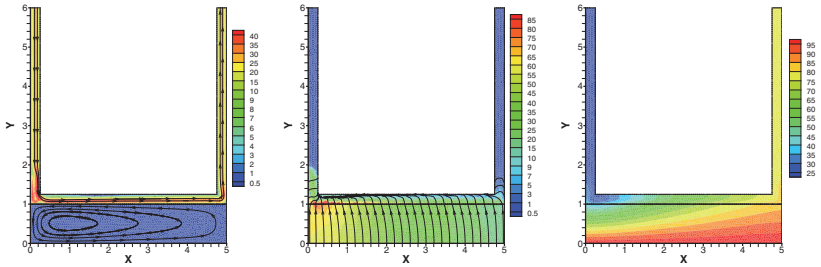

FIG. 5.6. *Numerical results for $Ra = 10^4$, $Pr = 3.0$, $k_f = 0.6$, $k_p = 1.0$, $Da = 1.0 \times 10^{-6}$, and $T = 3.0$. Left: streamlines and magnitudes of velocity. Middle: streamlines and magnitudes of heat flux. Right: temperature distribution.*

Figure 5.7 shows the temperature distribution at different times to illustrate the effect of the geothermal energy with respect to the time. The pictures show that with the increase of the time, the thermal convection and the temperature of the outflow gradually increase to the maximum. During this procedure, the transmission area from cold water to hot water becomes smaller and closer to the corner between the injection well and the horizontal well, while the production temperature is higher and higher as expected.

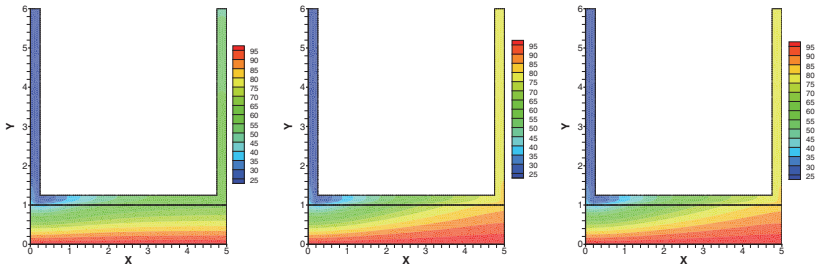

FIG. 5.7. *Temperature distribution at different times with* $Ra = 10^4$, $Pr = 3.0$, $k_f = 0.6$, $k_p = 1.0$, *and* $Da = 1.0 \times 10^{-6}$. *Left:* $T = 1.0$. *Middle:* $T = 3.0$. *Right:* $T = 10.0$.

Figure 5.8 shows temperature distribution for the different values of the Darcy number. The results clearly illustrate the effect of the porous media flow in the geothermal reservoir on the production temperature. When the Darcy number is decreased, the porous media flow becomes slower, hence leading to a slower heat transfer from the bottom of Ω_p to the area around the interface. This causes the less heat communication on the interface and eventually lower production temperature.

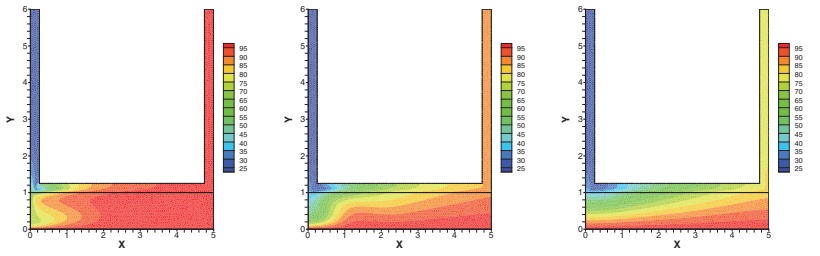

FIG. 5.8. *Temperature distribution with different values of Darcy number* Da, $Ra = 10^4$, $Pr = 3.0$, $k_f = 0.6$, $k_p = 1.0$, *and* $T = 3$. *Left:* $Da = 1.0 \times 10^{-3}$. *Middle:* $Da = 1.0 \times 10^{-4}$. *Right:* $Da = 1.0 \times 10^{-5}$.

Figure 5.9 shows the effect of different values of thermal conductivity. One can obviously observe that the larger heat conductivity in the reservoir leads to a faster heat convection, hence a faster change of the working fluid temperature to the maximum. With the large heat conductivity $k_p = 1.5$, some fluid in the left vertical well is even heated up before it gets close to the horizontal well, which does not happen much when k_p is 0.6 or 1.0.

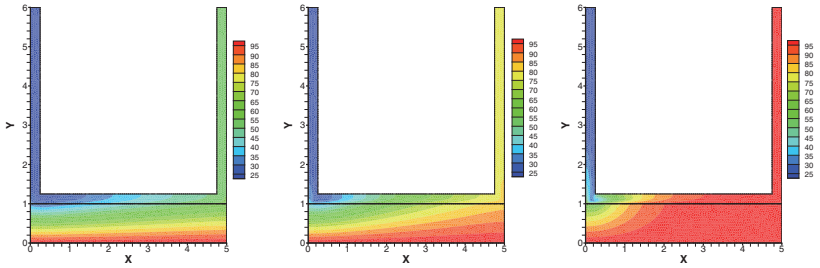

FIG. 5.9. *Temperature distribution with different values of thermal conductivity* k_p, $Ra = 10^4$, $Pr = 3.0$, $k_f = 0.6$, $Da = 1.0 \times 10^{-6}$, *and* $T = 3.0$. *Left:* $k_p = 0.6$. *Middle:* $k_p = 1.0$. *Right:* $k_p = 1.5$.

Figures 5.10 and 5.11 show the effect of different lengths of the horizontal wellbore and different injection temperatures, respectively. While the temperature distributions are in a similar pattern for different lengths of the horizontal wellbore, the production temperature is lower with respect to the shorter horizontal well due to the less heat flux communication on the interface. As expected, the higher injection temperature causes a faster procedure for the working fluid to reach its maximum temperature and provides higher production temperature.

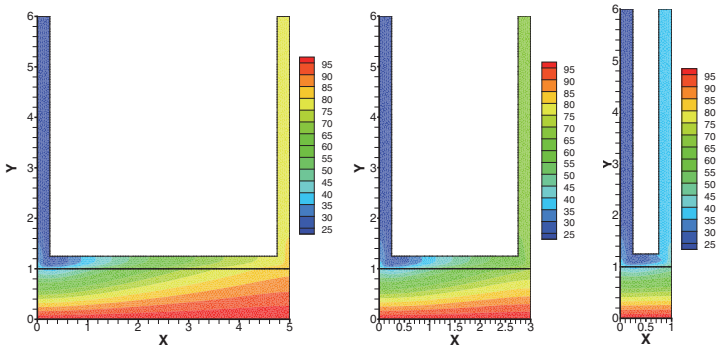

FIG. 5.10. *Temperature distribution with different lengths of the horizontal well,* $Ra = 10^4$, $Pr = 3.0$, $k_f = 0.6$, $k_p = 1.0$, $Da = 1.0 \times 10^{-6}$, *and* $T = 3.0$. *Left: length* $= 5.0$. *Middle: length* $= 3.0$. *Right: length* $= 1.0$.

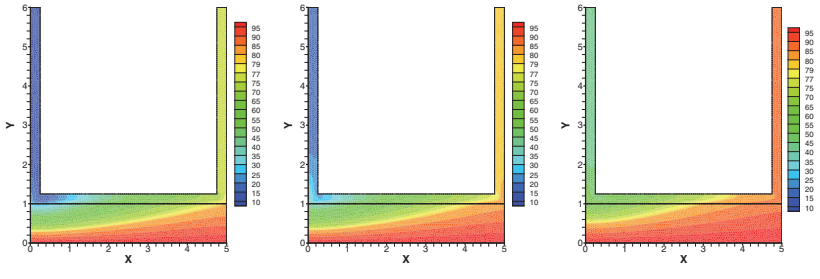

FIG. 5.11. *Temperature distribution with different inflow temperatures,* $Ra = 10^4$, $Pr = 3.0$, $k_f = 0.6$, $k_p = 1.0$, $Da = 1.0 \times 10^{-6}$, *and* $T = 3.0$. *Left: injection temperature* $= 5$. *Middle: injection temperature* $= 20$. *Right: injection temperature* $= 45$.

5.4. Simulation for a closed-loop geothermal system with curved interface. In this example, we simulate the thermal convection in a simplified closed-loop geothermal system with curved interface. One difference between this example and the previous one is that the curved heat exchange pipeline is immersed in the geothermal reservoir.

The computational domain is illustrated in Figure 5.12. We assume a hot wall situation by imposing $\theta_p = 120$ on the boundaries $\{(x, y) : y = 0, 0 \leqslant x \leqslant 6\} \subset \partial\Omega_p$ and $\{(x, y) : y = 3, 0.25 \leqslant x \leqslant 5.75\} \subset \partial\Omega_p$, which are the bottom and top sides of the geothermal reservoir. The no-flow boundary condition $\vec{u}_p \cdot \hat{n}_p = 0$ is imposed on the other boundaries of the reservoir $\partial\Omega_p \setminus \mathbb{I}$. We assume the homogeneous Neumann boundary condition for the temperature on the left and right walls of Ω_p. The initial condition for the velocity and temperature in the geothermal reservoir is considered as $\vec{u}_p(0, x) = (0, 0)$ and $\theta_p(0, x) = 120$.

On the top boundary $\partial\Omega_{f\,\text{in}} = \{(x, y) : y = 7, 0 \leqslant x \leqslant 0.25\}$ of the vertical injection well, we consider the inflow boundary condition by assuming $U_x = 0$ and $U_y = -2048.0x(0.25 - x)$. The boundary condition for temperature is assumed as $\theta_f = 20$ on the same boundary. The initial condition for the velocity and temperature of the closed-loop pipe is assumed as $\vec{u}_f(0, x) = (0, 0)$ and $\theta_f(0, x) = 20$, respectively. On the top boundary $\partial\Omega_{f\,\text{out}} = \{(x, y) : y = 7, 5.75 \leqslant x \leqslant 6\}$ of the vertical production well on the right, the free outflow boundary condition is imposed:

$$(-p_f \mathbf{I} + Pr\nabla\vec{u}_f) \cdot \hat{n}_f = 0, \qquad \hat{n}_f \cdot k_f \nabla\theta_f = 0 \quad \text{on} \quad \partial\Omega_{f\,\text{out}}. \tag{5.5}$$

On the other boundaries belonging to $\partial\Omega_f \setminus \mathbb{I}$, the no-slip boundary condition for velocity and the insulated boundary condition for temperature are considered:

$$\vec{u}_f = 0, \qquad \hat{n}_f \cdot k_f \nabla\theta_f = 0 \quad \text{on } \partial\Omega_f \setminus \mathbb{I}. \tag{5.6}$$

The proposed interface conditions (2.20)–(2.23) are used on the interface $\mathbb{I}$ between the geothermal reservoir and pipe. For the fundamental simulation, the parameter values are chosen as $k_f = 0.6$, $k_p = 1.0$, $Pr = 3.0$, $Ra = 10^4$, $C_a = 1.0$, $Da = 1.0 \times 10^{-7}$, and $\gamma = 1.0$. The mesh size $h_{max} = 0.05$, temporal step size $\Delta t = 0.05$, and final time $T = 5.0$ are considered for the current computation. The external body forces $\vec{f}_f$, Υ_f, and Υ_p are simply taken as zero.

In Figure 5.13, we present the influence of the different values of thermal conductivity on the temperature distribution. As expected, the larger heat conductivity in the reservoir leads to faster heat convection, which provides the faster change of

the fluid in the pipe to the maximum temperature. Furthermore, Figure 5.14 demonstrates the effects of the different shapes of the interface on the heat transfer. Figure 5.15 shows the temperature distribution for different boundary values of θ_p on the top and bottom boundaries of the geothermal reservoir, which represent the reservoir temperature. As expected, the hotter reservoir produces more energy, which can be seen by the temperature in the vertical production wellbore.

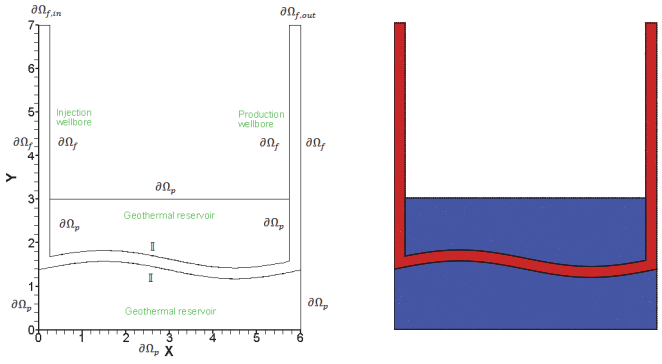

FIG. 5.12. *The U-shape domain consists of closed-loop heat exchanging pipelines Ω_f and geothermal reservoir Ω_p, separated by the curved interface $\mathbb{I}$ (left) and illustration of mesh (right).*

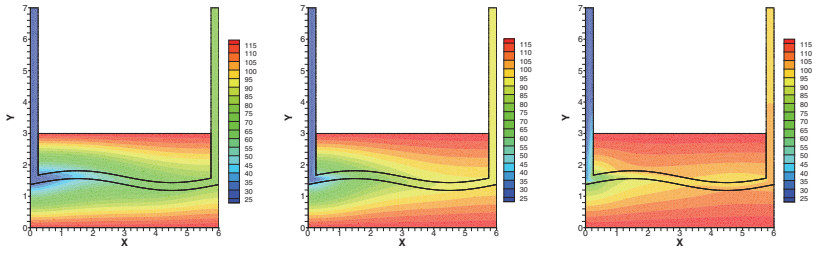

FIG. 5.13. *Temperature distribution with different values of thermal conductivity k_p, $Ra = 10^4$, $Pr = 3.0$, $k_f = 0.6$, $Da = 1.0 \times 10^{-7}$, and $T = 3.0$. Left: $k_p = 0.6$. Middle: $k_p = 1.0$. Right: $k_p = 1.5$.*

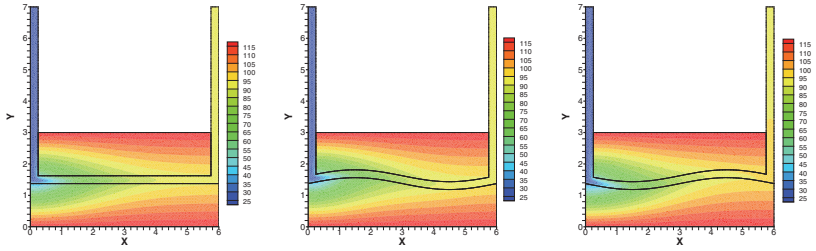

FIG. 5.14. *Temperature distribution with different shapes of the interface* $\mathbb{I}$, $Ra = 10^4$, $Pr = 3.0$, $k_f = 0.6$, $k_p = 1.0$, $Da = 1.0 \times 10^{-7}$, *and* $T = 3.0$. *Left: flat interface. Middle: concave to convex shape interface. Right: convex to concave shape interface.*

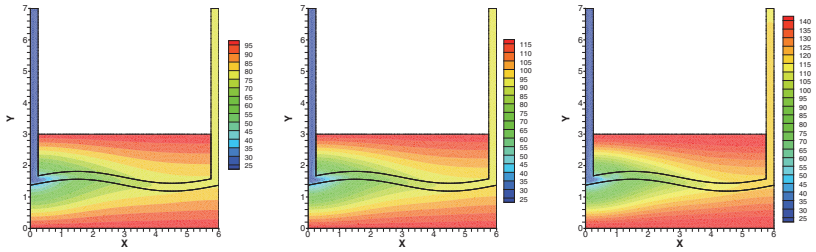

FIG. 5.15. *Temperature distribution with different* θ_p, $Ra = 10^4$, $Pr = 3.0$, $k_f = 0.6$, $k_p = 1.0$, $Da = 1.0 \times 10^{-7}$, *and* $T = 3.0$. *Left:* $\theta_p = 100.0$. *Middle:* $\theta_p = 120.0$. *Right:* $\theta_p = 150.0$.

6. Conclusion. In this paper, a coupled multiphysics model is proposed for the closed-loop type geothermal system. In a network of a underground heat exchanging pipelines, the free flow is governed by a Boussinesq equation which combines the Navier–Stokes equation coupled with the heat equation. In the geothermal reservoir, the porous media flow is governed by Darcy's law coupled with the heat equation. Since there is no-direct flow interaction but just heat transfer between the geothermal reservoir and the pipelines, four physically valid interface conditions are imposed to describe the no-communication feature of the fluid flow and continuous heat transfer of the heat flow. To solve the proposed model accurately and efficiently, we developed a decoupled stabilized finite element approach based on the traditional coupled finite element method. The stability of the coupled and decoupled schemes is reported. Four numerical experiments are provided to validate and illustrate the features of the proposed model and numerical method.

REFERENCES

[1] R. A. ADAMS AND J. J. F. FOURNIER, *Sobolev Spaces*, 2nd ed., Pure Appl. Math. (Amst.) 140, Elsevier/Academic Press, Amsterdam, 2003.

[2] S. ADJERID, R. GUO, AND T. LIN, *High degree immersed finite element spaces by a least squares method*, Int. J. Numer. Anal. Model., 14 (2017), pp. 604–626.

[3] M. D. ALIYU AND H.-P. CHEN, *Sensitivity analysis of deep geothermal reservoir: Effect of reservoir parameters on production temperature*, Energy, 129 (2017), pp. 101–113.

[4] K. ALLALI, F. BIKANY, A. TAIK, AND V. VOLPERT, *Numerical simulations of heat explosion with convection in porous media*, Combust. Sci. Technol., 187 (2015), pp. 384–395.

[5] D. N. Arnold, F. Brezzi, and M. Fortin, *A stable finite element for the Stokes equations*, Calcolo, 21 (1984), pp. 337–344.
[6] L. Badea, M. Discacciati, and A. Quarteroni, *Numerical analysis of the Navier-Stokes/Darcy coupling*, Numer. Math., 115 (2010), pp. 195–227.
[7] J. Bai, Y. Cao, X.-M. He, H. Liu, and X. Yang, *Modeling and an immersed finite element method for an interface wave equation*, Comput. Math. Appl., 76 (2018), pp. 1625–1638.
[8] C. Bernardi, S. Dib, V. Girault, F. Hecht, F. Murat, and T. Sayah, *Finite element methods for Darcy's problem coupled with the heat equation*, Numer. Math., 139 (2018), pp. 315–348.
[9] C. Bernardi, S. Maarouf, and D. Yakoubi, *Spectral discretization of Darcy's equations coupled with the heat equation*, IMA J. Numer. Anal., 36 (2016), pp. 1193–1216.
[10] B. Bezyan, S. Porkhial, and A. A. Mehrizi, 3-*D simulation of heat transfer rate in geothermal pile-foundation heat exchangers with spiral pipe configuration*, Appl. Therm. Eng., 87 (2015), pp. 655–668.
[11] J. Boland and W. Layton, *An analysis of the finite element method for natural convection problems*, Numer. Methods Partial Differential Equations, 6 (1990), pp. 115–126.
[12] J. Boland and W. Layton, *Error analysis for finite element methods for steady natural convection problems*, Numer. Funct. Anal. Optim., 11 (1990), pp. 449–483.
[13] Y. Boubendir and S. Tlupova, *Stokes-Darcy boundary integral solutions using preconditioners*, J. Comput. Phys., 228 (2009), pp. 8627–8641.
[14] D. Bresch and J. Koko, *Operator-splitting and Lagrange multiplier domain decomposition methods for numerical simulation of two coupled Navier-Stokes fluids*, Int. J. Appl. Math. Comput. Sci., 16 (2006), pp. 419–429.
[15] F. Brezzi, J. Douglas, and L. D. Marini, *Two families of mixed elements for second order elliptic problems*, Numer. Math., 47 (1985), pp. 217–235.
[16] M. Bukač, I. Yotov, R. Zakerzadeh, and P. Zunino, *Partitioning strategies for the interaction of a fluid with a poroelastic material based on a Nitsche's coupling approach*, Comput. Methods Appl. Mech. Engrg., 292 (2015), pp. 138–170.
[17] J. Bundschuh and M. C. S. Arriaga, *Introduction to the Numerical Modeling of Groundwater and Geothermal Systems: Fundamentals of Mass, Energy and Solute Transport in Poroelastic Rocks*, CRC Press, Boca Raton, FL, 2010.
[18] E. Burman and M. A. Fernández, *Stabilization of explicit coupling in fluid-structure interaction involving fluid incompressiblity*, Comput. Methods Appl. Mech. Engrg., 198 (2009), pp. 766–784.
[19] J. A. Burns, X.-M. He, and W. Hu, *Feedback stabilization of a thermal fluid system with mixed boundary control, in honor of Max Gunzburger's* 70*th birthday*, Comput. Math. Appl., 71 (2016), pp. 2170–2191.
[20] M. Cai, M. Mu, and J. Xu, *Numerical solution to a mixed Navier–Stokes/Darcy model by the two-grid approach*, SIAM J. Numer. Anal., 47 (2009), pp. 3325–3338, https://doi.org/10.1137/080721868.
[21] Y. Cao, Y. Chu, X.-M. He, and M. Wei, *Decoupling the stationary Navier-Stokes-Darcy system with the Beavers-Joseph-Saffman interface condition*, Abstr. Appl. Anal., (2013), 136483.
[22] Y. Cao, M. Gunzburger, X.-M. He, and X. Wang, *Robin-Robin domain decomposition methods for the steady-state Stokes-Darcy system with the Beavers-Joseph interface condition*, Numer. Math., 117 (2011), pp. 601–629.
[23] Y. Cao, M. Gunzburger, X.-M. He, and X. Wang, *Parallel, non-iterative, multi-physics domain decomposition methods for time-dependent Stokes-Darcy systems*, Math. Comp., 83 (2014), pp. 1617–1644.
[24] Y. Cao, M. Gunzburger, X. Hu, F. Hua, X. Wang, and W. Zhao, *Finite element approximation for Stokes-Darcy flow with Beavers-Joseph interface conditions*, SIAM. J. Numer. Anal., 47 (2010), pp. 4239–4256, https://doi.org/10.1137/080731542.
[25] A. Çeşmelioğlu, V. Girault, and B. Rivière, *Time-dependent coupling of Navier-Stokes and Darcy flows*, ESAIM Math. Model. Numer. Anal., 47 (2013), pp. 539–554.
[26] A. Çeşmelioğlu and B. Rivière, *Analysis of time-dependent Navier-Stokes flow coupled with Darcy flow*, J. Numer. Math., 16 (2008), pp. 249–280.
[27] A. Çeşmelioğlu and B. Rivière, *Primal discontinuous Galerkin methods for time-dependent coupled surface and subsurface flow*, J. Sci. Comput., 40 (2009), pp. 115–140.
[28] S. Chandrasekhar, *Hydrodynamic and Hydromagnetic Stability*, Dover, Mineola, NY, 1961.
[29] J. Chen, S. Sun, and X. Wang, *A numerical method for a model of two-phase flow in a coupled free flow and porous media system*, J. Comput. Phys., 268 (2014), pp. 1–16.

[30] W. Chen, M. Gunzburger, F. Hua, and X. Wang, *A parallel Robin-Robin domain decomposition method for the Stokes-Darcy system*, SIAM. J. Numer. Anal., 49 (2011), pp. 1064–1084, https://doi.org/10.1137/080740556.

[31] W. Chen, D. Han, and X. Wang, *Uniquely solvable and energy stable decoupled numerical schemes for the Cahn-Hilliard-Stokes-Darcy system for two-phase flows in karstic geometry*, Numer. Math., 137 (2017), pp. 229–255.

[32] Z. Chen and J. Zou, *Finite element methods and their convergence for elliptic and parabolic interface problems*, Numer. Math., 79 (1998), pp. 175–202.

[33] P. Chidyagwai and B. Rivière, *On the solution of the coupled Navier-Stokes and Darcy equations*, Comput. Methods Appl. Mech. Engrg., 198 (2009), pp. 3806–3820.

[34] J. C. Choi, J. Park, and S. R. Lee, *Numerical evaluation of the effects of groundwater flow on borehole heat exchanger arrays*, Renewable Energy, 52 (2013), pp. 230–240.

[35] W. Choi and R. Ooka, *Effect of natural convection on thermal response test conducted in saturated porous formation: Comparison of gravel-backfilled and cement-grouted borehole heat exchangers*, Renewable Energy, 96 (2016), pp. 891–903.

[36] J. M. Connors and B. Ganis, *Stability of algorithms for a two domain natural convection problem and observed model uncertainty*, Comput. Geosci., 15 (2011), pp. 509–527.

[37] J. M. Connors, J. S. Howell, and W. J. Layton, *Decoupled time stepping methods for fluid-fluid interaction*, SIAM J. Numer. Anal., 50 (2012), pp. 1297–1319, https://doi.org/10.1137/090773362.

[38] R. Curtis, J. Lund, B. Sanner, L. Rybach, and G. Hellström, *Ground source heat pumps-geothermal energy for anyone, anywhere: Current worldwide activity*, in Proceedings of the World Geothermal Congress, Antalya, Turkey, 2005.

[39] J. Deteix, A. Jendoubi, and D. Yakoubi, *A coupled prediction scheme for solving the Navier-Stokes and convection-diffusion equations*, SIAM J. Numer. Anal., 52 (2014), pp. 2415–2439, https://doi.org/10.1137/130942516.

[40] A. E. Diegel, X. Feng, and S. M. Wise, *Analysis of a mixed finite element method for a Cahn-Hilliard-Darcy-Stokes system*, SIAM J. Numer. Anal., 53 (2015), pp. 127–152, https://doi.org/10.1137/130950628.

[41] M. Discacciati, *Domain Decomposition Methods for the Coupling of Surface and Groundwater Flows*, Ph.D. thesis, Ecole Polytechnique Fédérale de Lausanne, Lausanne, Switzerland, 2004.

[42] M. Discacciati, E. Miglio, and A. Quarteroni, *Mathematical and numerical models for coupling surface and groundwater flows*, Appl. Numer. Math., 43 (2002), pp. 57–74.

[43] M. Discacciati and A. Quarteroni, *Navier-Stokes/Darcy coupling: Modeling, analysis, and numerical approximation*, Rev. Mat. Comput., 22 (2009), pp. 315–426.

[44] M. Discacciati, A. Quarteroni, and A. Valli, *Robin-Robin domain decomposition methods for the Stokes-Darcy coupling*, SIAM J. Numer. Anal., 45 (2007), pp. 1246–1268, https://doi.org/10.1137/06065091X.

[45] S. Erol and B. Francois, *Multilayer analytical model for vertical ground heat exchanger with groundwater flow*, Geothermics, 71 (2018), pp. 294–305.

[46] R. E. Ewing, O. Iliev, and R. D. Lazarov, *A modified finite volume approximation of second-order elliptic equations with discontinuous coefficients*, SIAM J. Sci. Comput., 23 (2001), pp. 1335–1351, https://doi.org/10.1137/S1064827599353877.

[47] W. Feng, X.-M. He, Z. Wang, and X. Zhang, *Non-iterative domain decomposition methods for a non-stationary Stokes-Darcy model with Beavers-Joseph interface condition*, Appl. Math. Comput., 219 (2012), pp. 453–463.

[48] M. A. Fernández, J. F. Gerbeau, and S. Smaldone, *Explicit coupling schemes for a fluid-fluid interaction problem arising in hemodynamics*, SIAM J. Sci. Comput., 36 (2014), pp. A2557–A2583, https://doi.org/10.1137/130948653.

[49] C. Foias, O. Manley, and R. Temam, *Attractors for the Bénard problem: Existence and physical bounds on their fractal dimension*, Nonlinear Anal., 11 (1987), pp. 939–967.

[50] G. P. Galdi, *An Introduction to the Mathematical Theory of the Navier-Stokes Equations*, Vol. 1, Springer Tracts Nat. Philos. 38, Springer, New York, 1994.

[51] J. Galvis and M. Sarkis, *Non-matching mortar discretization analysis for the coupling Stokes-Darcy equations*, Electron. Trans. Numer. Anal., 26 (2007), pp. 350–384.

[52] Y. Gao, X.-M. He, L. Mei, and X. Yang, *Decoupled, linear, and energy stable finite element method for the Cahn–Hilliard–Navier–Stokes–Darcy phase field model*, SIAM J. Sci. Comput., 40 (2018), pp. B110–B137, https://doi.org/10.1137/16M1100885.

[53] G. N. Gatica, S. Meddahi, and R. Oyarzúa, *A conforming mixed finite-element method for the coupling of fluid flow with porous media flow*, IMA J. Numer. Anal., 29 (2009), pp. 86–108.

[54] G. N. Gatica, R. Oyarzúa, and F. J. Sayas, *A residual-based a posteriori error estimator for a fully-mixed formulation of the Stokes-Darcy coupled problem*, Comput. Methods Appl. Mech. Engrg., 200 (2011), pp. 1877–1891.
[55] V. Girault and P. A. Raviart, *Finite Element Approximations of the Navier-Stokes Equations*, Springer-Verlag, Berlin, 1986.
[56] V. Girault and B. Rivière, *DG approximation of coupled Navier-Stokes and Darcy equations by Beaver–Joseph–Saffman interface condition*, SIAM J. Numer. Anal, 47 (2009), pp. 2052–2089, https://doi.org/10.1137/070686081.
[57] Y. Gong and Z. Li, *Immersed interface finite element methods for elasticity interface problems with non-homogeneous jump conditions*, Numer. Math. Theory Methods Appl., 3 (2010), pp. 23–39.
[58] M. Gunzburger, X.-M. He, and B. Li, *On Stokes–Ritz projection and multistep backward differentiation schemes in decoupling the Stokes–Darcy model*, SIAM J. Numer. Anal., 56 (2018), pp. 397–427, https://doi.org/10.1137/16M1099601.
[59] D. Han, P. Wang, X.-M. He, T. Lin, and J. Wang, *A 3D immersed finite element method with non-homogeneous interface flux jump for applications in particle-in-cell simulations of plasma-lunar surface interactions*, J. Comput. Phys., 321 (2016), pp. 965–980.
[60] P. Hansbo, *Nitsche's method for interface problems in computational mechanics*, GAMM-Mitt., 28 (2005), pp. 183–206.
[61] P. Hansbo and J. Hermansson, *Nitsche's method for coupling non-matching meshes in fluid-structure vibration problems*, Comput. Mech., 32 (2003), pp. 134–139.
[62] N. Hanspal, A. Waghode, V. Nassehi, and R. Wakeman, *Numerical analysis of coupled Stokes/Darcy flow in industrial filtrations*, Transp. Porous Media, 64 (2006), pp. 73–101.
[63] X.-M. He, *Bilinear Immersed Finite Elements for Interface Problems*, Ph.D. Dissertation, Virginia Polytechnic Institute and State University, 2009, Blacksburg, VA.
[64] X.-M. He, N. Jiang, and C. Qiu, *An artificial compressibility ensemble algorithm for a stochastic Stokes-Darcy model with random hydraulic conductivity and interface conditions*, Internat. J. Numer. Methods Engrg., 121 (2020), pp. 712–739.
[65] X.-M. He, J. Li, Y. Lin, and J. Ming, *A domain decomposition method for the steady-state Navier–Stokes–Darcy model with Beavers–Joseph interface condition*, SIAM J. Sci. Comput., 37 (2015), pp. S264–S290, https://doi.org/10.1137/140965776.
[66] X.-M. He, T. Lin, and Y. Lin, *Approximation capability of a bilinear immersed finite element space*, Numer. Methods Partial Differential Equations, 24 (2008), pp. 1265–1300.
[67] X.-M. He, T. Lin, and Y. Lin, *Immersed finite element methods for elliptic interface problems with non-homogeneous jump conditions*, Int. J. Numer. Anal. Model., 8 (2011), pp. 284–301.
[68] X.-M. He, T. Lin, and Y. Lin, *The convergence of the bilinear and linear immersed finite element solutions to interface problems*, Numer. Methods Partial Differential Equations, 28 (2012), pp. 312–330.
[69] X.-M. He, T. Lin, Y. Lin, and X. Zhang, *Immersed finite element methods for parabolic equations with moving interface*, Numer. Methods Partial Differential Equations, 29 (2013), pp. 619–646.
[70] J. Hecht-Méndez, M. D. Paly, M. Beck, and P. Bayer, *Optimization of energy extraction for vertical closed-loop geothermal systems considering groundwater flow*, Energy Conversion and Management, 66 (2013), pp. 1–10.
[71] J. G. Heywood and R. Rannacher, *Finite element approximation of the nonstationary Navier–Stokes problem, Part* IV: *Error analysis for second-order time discretization*, SIAM J. Numer. Anal., 27 (1990), pp. 353–384, https://doi.org/10.1137/0727022.
[72] S. C. Hirata, B. Goyeau, D. Gobin, M. Carr, and R. M. Cotta, *Linear stability of natural convection in superposed fluid and porous layers: Influence of the interfacial modeling*, Int. J. Heat Mass Transfer, 50 (2007), pp. 1356–1367.
[73] R. Hoppe, P. Porta, and Y. Vassilevski, *Computational issues related to iterative coupling of subsurface and channel flows*, Calcolo, 44 (2007), pp. 1–20.
[74] J. Hou, M. Qiu, X.-M. He, C. Guo, M. Wei, and B. Bai, *A dual-porosity-Stokes model and finite element method for coupling dual-porosity flow and free flow*, SIAM J. Sci. Comput., 38 (2016), pp. B710–B739, https://doi.org/10.1137/15M1044072.
[75] H. Kaydani and A. Mohebbi, *Experimental and numerical study of the onset of transient natural convection in a fractured porous medium*, Transp. Porous Med., 116 (2017), pp. 923–939.
[76] W. Layton, H. Tran, and C. Trenchea, *Analysis of long time stability and errors of two partitioned methods for uncoupling evolutionary groundwater–surface water flows*, SIAM J. Numer. Anal., 51 (2013), pp. 248–272, https://doi.org/10.1137/110834494.

[77] W. J. Layton, F. Schieweck, and I. Yotov, *Coupling fluid flow with porous media flow*, SIAM J. Numer. Anal., 40 (2002), pp. 2195–2218, https://doi.org/10.1137/S0036142901392766.
[78] H.-C. Lee, *Analysis and computational methods of Dirichlet boundary optimal control problems for 2D Boussinesq equations*, Adv. Comput. Math., 19 (2003), pp. 255–275.
[79] R. J. LeVeque and Z. Li, *The immersed interface method for elliptic equations with discontinuous coefficients and singular sources*, SIAM J. Numer. Anal., 34 (1994), pp. 1019–1044, https://doi.org/10.1137/0731054.
[80] M. Lin, T. Lin, and H. Zhang, *Error analysis of an immersed finite element method for Euler-Bernoulli beam interface problems*, Int. J. Numer. Anal. Model., 14 (2017), pp. 822–841.
[81] T. Lin, D. Sheen, and X. Zhang, *A locking-free immersed finite element method for planar elasticity interface problems*, J. Comput. Phys., 247 (2013), pp. 228–247.
[82] J. W. Lund and T. L. Boyd, *Direct utilization of geothermal energy* 2015 *worldwide review*, Geothermics, 60 (2016), pp. 66–93.
[83] F. Luo, R.-N. Xu, and P.-X. Jiang, *Numerical study of the influence of injection/production well perforation location on CO_2-EGS system*, Energy Procedia, 37 (2013), pp. 6636–6643.
[84] M. A. A. Mahbub, X.-M. He, N. J. Nasu, C. Qiu, and H. Zheng, *Coupled and decoupled stabilized mixed finite element methods for non-stationary dual-porosity-Stokes fluid flow model*, Internat. J. Numer. Methods Engrg., 120 (2019), pp. 803–833.
[85] A. Márquez, S. Meddahi, and F. J. Sayas, *A decoupled preconditioning technique for a mixed Stokes-Darcy model*, J. Sci. Comput., 57 (2013), pp. 174–192.
[86] A. Massing, M. G. Larson, A. Logg, and M. G. Rognes, *A stabilized Nitsche overlapping mesh method for the Stokes problem*, Numer. Math., 128 (2014), pp. 73–101.
[87] M. Mu and J. Xu, *A two-grid method of a mixed Stokes–Darcy model for coupling fluid flow with porous media flow*, SIAM J. Numer. Anal., 45 (2007), pp. 1801–1813, https://doi.org/10.1137/050637820.
[88] S. Münzenmaier and G. Starke, *First-order system least squares for coupled Stokes–Darcy flow*, SIAM J. Numer. Anal., 49 (2011), pp. 387–404, https://doi.org/10.1137/100805108.
[89] M. Nabi and R. Al-Khoury, *An efficient finite volume model for shallow geothermal systems, Part* I: *Model formulation*, Comput. Geosci., 49 (2012), pp. 290–296.
[90] D. A. Nield and A. Bejan, *Convection in Porous Media*, Springer-Verlag, New York, 2006.
[91] J. Nitsche, *Über ein Variationsprinzip zur Lösung von Dirichlet-Problemen bei Verwendung von Teilräumen, die keinen Randbedingungen unterworfen sind*, Abh. Math. Sem. Univ. Hamburg, 36 (1971), pp. 9–15.
[92] C. M. Oldenburg, L. Pan, M. P. Muir, A. D. Eastman, and B. S. Higgins, *Numerical simulation of critical factors controlling heat extraction from geothermal systems using a closed-loop heat exchange method*, in Proceedings of the 41st Workshop on Geothermal Reservoir Engineering, Stanford University, Stanford, CA, 2016, pp. 1–8.
[93] X. Pan, K. Kim, C. Lee, and J.-I. Choi, *A decoupled monolithic projection method for natural convection problems*, J. Comput. Phys., 314 (2016), pp. 160–166.
[94] C. Qiu, X.-M. He, J. Li, and Y. Lin, *A domain decomposition method for the time-dependent Navier-Stokes-Darcy model with Beavers-Joseph interface condition and defective boundary condition*, J. Comput. Phys., 411 (2020), 109400.
[95] A. Riahi, P. Moncarz, W. Kolbe, and B. Damjanac, *Innovative closed-loop geothermal well designs using water and super critical carbon dioxide as working fluids*, in Proceedings of the 42nd Workshop on Geothermal Reservoir Engineering, Stanford University, Stanford, CA, 2017, pp. 1–9.
[96] B. Rivière and I. Yotov, *Locally conservative coupling of Stokes and Darcy flows*, SIAM J. Numer. Anal., 42 (2005), pp. 1959–1977, https://doi.org/10.1137/S0036142903427640.
[97] I. Rybak and J. Magiera, *A multiple-time-step technique for coupled free flow and porous medium systems*, J. Comput. Phys., 272 (2014), pp. 327–342.
[98] L. Shan and Y. Hou, *A fully discrete stabilized finite element method for the time-dependent Navier-Stokes equations*, Appl. Math. Comput., 215 (2009), pp. 85–99.
[99] D. C. Smith, A. C. Elmore, and J. Thompson, *The effect of seasonal groundwater saturation on the effectiveness of large scale borehole heat exchangers in a karstic aquifer*, Geothermics, 75 (2018), pp. 164–170.
[100] S. K. F. Stoter, P. Müller, L. Cicalese, M. Tuveri, D. Schillinger, and T. J. R. Hughes, *A diffuse interface method for the Navier-Stokes/Darcy equations: Perfusion profile for a patient-specific human liver based on MRI scans*, Comput. Methods Appl. Mech. Engrg., 321 (2017), pp. 70–102.

[101] R. Temam, *Navier-Stokes Equations: Theory and Numerical Analysis*, AMS Chelsea Publishing, Providence, RI, 2001.
[102] V. Thomée, *Galerkin Finite Element Methods for Parabolic Problems*, Springer Ser. Comput. Math. 25, Springer-Verlag, Berlin, 1997.
[103] S. Vallaghè and T. Papadopoulo, *A trilinear immersed finite element method for solving the electroencephalography forward problem*, SIAM J. Sci. Comput., 32 (2010), pp. 2379–2394, https://doi.org/10.1137/09075038X.
[104] D. Vassilev and I. Yotov, *Coupling Stokes–Darcy flow with transport*, SIAM J. Sci. Comput., 31 (2009), pp. 3661–3684, https://doi.org/10.1137/080732146.
[105] D. C. Wan, B. S. V. Patnaik, and G. W. Wei, *A new benchmark quality solution for the buoyancy-driven cavity by discrete singular convolution*, Numer. Heat Transfer, Part B, 40 (2001), pp. 199–228.
[106] H. Wang, C. Qi, H. Du, and J. Gu, *Thermal performance of borehole heat exchanger under groundwater flow: A case study from Baoding*, Energy and Buildings, 41 (2009), pp. 1368–1373.
[107] B. Wu, T. Ma, G. Feng, Z. Chen, and X. Zhang, *An approximate solution for predicting the heat extraction and preventing heat loss from a closed-loop geothermal reservoir*, Geofluids, 2017 (2017), pp. 1–17.
[108] Y. Zhang, Y. Hou, and J. Zhao, *Error analysis of a fully discrete finite element variational multiscale method for the natural convection problem*, Comput. Math. Appl., 68 (2014), pp. 543–567.
[109] Y. Zhang, Y. Hou, and H. Zheng, *A finite element variational multiscale method for steady-state natural convection problem based on two local Gauss integrations*, Numer. Methods Partial Differential Equations, 30 (2014), pp. 361–375.